Article

Cell

Crystal Structure of an LSD-Bound Human Serotonin Receptor

Graphical Abstract

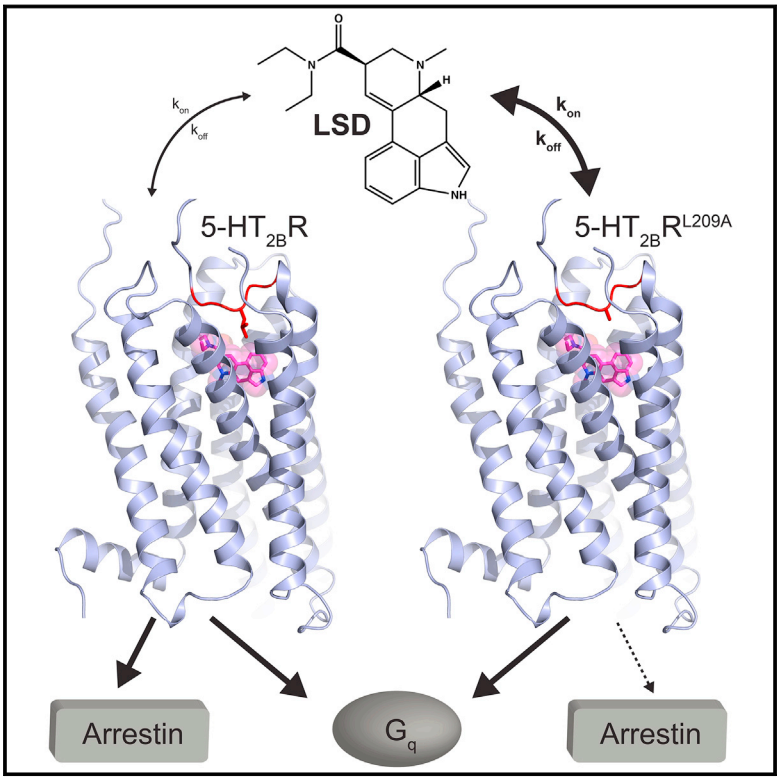

Authors

Daniel Wacker, Sheng Wang, John D. McCorvy, ..., Brian K. Shoichet, Ron O. Dror, Bryan L. Roth

Correspondence

dwacker@email.unc.edu (D.W.), ron.dror@stanford.edu (R.O.D.), bryan_roth@med.unc.edu (B.L.R.)

In Brief

The structure of LSD with a serotonin receptor reveals the basis for its long-lasting effects and suggests ways to selectively alter receptor signaling.

Highlights

- Crystal structure of the human 5-HT$_{2B}$ receptor bound to LSD is determined
- LSD shows unexpected binding configuration in the orthosteric site
- LSD has extremely slow on and off rate at 5-HT$_{2B}$ and 5-HT$_{2A}$ receptors
- Accelerated LSD kinetics selectively reduce arrestin signaling at 5-HT$_{2B}$ and 5-HT$_{2A}$

Data Resources

5TVN

Wacker et al., 2017, Cell *168*, 377–389
January 26, 2017
http://dx.doi.org/10.1016/j.cell.2016.12.033

CellPress

Cell

Crystal Structure of an LSD-Bound Human Serotonin Receptor

Daniel Wacker,[1,9,*] Sheng Wang,[1,9] John D. McCorvy,[1,9] Robin M. Betz,[2,3,4,5] A.J. Venkatakrishnan,[2,3,4] Anat Levit,[6] Katherine Lansu,[1] Zachary L. Schools,[1] Tao Che,[1] David E. Nichols,[7] Brian K. Shoichet,[6] Ron O. Dror,[2,3,4,5,*] and Bryan L. Roth[1,7,8,10,*]

[1]Department of Pharmacology, University of North Carolina at Chapel Hill School of Medicine, Chapel Hill, NC 27599-7365, USA
[2]Department of Computer Science, Stanford University, Stanford, CA 94305, USA
[3]Department of Molecular and Cellular Physiology, Stanford University School of Medicine, Stanford, CA 94305, USA
[4]Institute for Computational and Mathematical Engineering, Stanford University, Stanford, CA 94305, USA
[5]Biophysics Program, Stanford University, Stanford, CA 94305, USA
[6]Department of Pharmaceutical Chemistry, University of California, San Francisco, San Francisco, CA 94158-2280, USA
[7]Division of Chemical Biology and Medicinal Chemistry, Eshelman School of Pharmacy, University of North Carolina at Chapel Hill, Chapel Hill, NC 27599-7360, USA
[8]National Institute of Mental Health Psychoactive Drug Screening Program (NIMH PDSP), School of Medicine, University of North Carolina at Chapel Hill School of Medicine, Chapel Hill, NC 27599-7365, USA
[9]Co-first author
[10]Lead Contact
*Correspondence: dwacker@email.unc.edu (D.W.), ron.dror@stanford.edu (R.O.D.), bryan_roth@med.unc.edu (B.L.R.)
http://dx.doi.org/10.1016/j.cell.2016.12.033

SUMMARY

The prototypical hallucinogen LSD acts via serotonin receptors, and here we describe the crystal structure of LSD in complex with the human serotonin receptor 5-HT_{2B}. The complex reveals conformational rearrangements to accommodate LSD, providing a structural explanation for the conformational selectivity of LSD's key diethylamide moiety. LSD dissociates exceptionally slow from both 5-HT_{2B}R and 5-HT_{2A}R—a major target for its psychoactivity. Molecular dynamics (MD) simulations suggest that LSD's slow binding kinetics may be due to a "lid" formed by extracellular loop 2 (EL2) at the entrance to the binding pocket. A mutation predicted to increase the mobility of this lid greatly accelerates LSD's binding kinetics and selectively dampens LSD-mediated β-arrestin2 recruitment. This study thus reveals an unexpected binding mode of LSD; illuminates key features of its kinetics, stereochemistry, and signaling; and provides a molecular explanation for LSD's actions at human serotonin receptors.

INTRODUCTION

Lysergic acid diethylamide (LSD) is not only the prototypical human hallucinogen, but also one of the most potent known psychoactive drugs. LSD was synthesized in 1938 by Albert Hofmann, who in 1943 accidently discovered its potent hallucinogenic properties (Hofmann, 1979). LSD alters human perception and mood (Nichols, 2016) and users report profound psychological experiences, or "trips," lasting 6–15 hr (Passie et al., 2008). LSD gained popularity as a legal recreational drug in the early 1960's, although it was soon classified as a schedule 1 controlled substance. A renewed scientific interest in LSD not only provides support for its potential application in disorders such as substance abuse (Bogenschutz and Johnson, 2016), cluster headaches (Sewell et al., 2006), and anxiety associated with life-threatening conditions (Gasser et al., 2015), but also has illustrated LSD's potential utility in studying aspects of human psychopathology and consciousness (Carhart-Harris et al., 2016). LSD has a complex pharmacology, exhibiting potent interactions with essentially all aminergic G-protein-coupled receptors (GPCRs) (Kroeze et al., 2015; Roth et al., 2002)—including all 13 human serotonergic GPCRs (Roth et al., 2002; Wacker et al., 2013; Wang et al., 2013). LSD appears to manifest its psychoactive properties primarily through 5-HT2-family serotonin receptors, in particular at the 5-HT_{2A} receptor (5-HT_{2A}R) (Titeler et al., 1988), which is enriched in cortical layer V pyramidal neurons (Jakab and Goldman-Rakic, 1998). LSD is a semi-synthetic member of a larger class of ergolines that have long been recognized as therapeutics for many conditions, including migraine headaches, post-partum hemorrhage, and Parkinson's disease (Berger et al., 2009).

It is well known that LSD activates canonical G-protein-mediated signaling at many GPCRs, but it has only recently been appreciated that LSD also potently activates the non-canonical β-arrestin pathway at most biogenic amine GPCRs (Kroeze et al., 2015), including all but one serotonin receptor (Wacker et al., 2013; Wang et al., 2013). Whereas most endogenous agonists, such as serotonin, activate both G-protein and β-arrestin pathways, some compounds can stabilize distinct receptor conformations, thereby preferentially activating select signal transduction pathways. This phenomenon has been termed "functional selectivity" or "biased agonism" (Urban et al., 2007; Violin and Lefkowitz, 2007) and represents a promising avenue of drug development, as specific signaling pathways have been linked to both the beneficial (Allen et al., 2011) and deleterious effects (Manglik et al., 2016) of drugs. Although the

Table 1. Data Collection and Refinement Statistics

Structure	Human 5-HT_{2B}R (ΔN/ΔICL3$_{BRIL}$/ΔC)-LSD Complex
Data collection	APS, GMCA/CAT 23ID-B/D, 10-μm microfocus beam
Crystals	9
Resolution range	29.2–2.9 (3.0–2.9)
Space group	$C222_1$
Unit cell dimensions a, b, c (Å)	59.2 119.2 171.0
Total reflections	46,859 (4290)
Unique reflections	12,568 (1163)
Multiplicity	3.7 (3.6)
Completeness (%)	90.4 (92.2)
Mean I/σ(I)	6.2 (2.0)
R_{merge}[a] (%)	15.0 (75.4)
$CC_{1/2}$ (%)	98.4 (62.9)
CC* (%)	99.6 (87.9)
Refinement statistics	
Reflections used in refinement	12,393 (1,162)
Reflections used for R-free	638 (67)
R-work (%)	22.5 (28.4)
R-free (%)	26.6 (35.8)
CC-work (%)	93.7 (77.9)
CC-free (%)	87.4 (65.4)
Number of atoms	
5-HT_{2B}R	2218
BRIL	721
LSD	24
Lipid and other	60
Overall B factors (Å^2)	
5-HT_{2B}R	60.0
BRIL	70.0
LSD	55.3
Lipids and other	67.6
Model statistics	
RMSD bonds (Å)	0.003
RMSD angles (°)	0.94
Ramachandran favored (%)[b]	97
Ramachandran allowed (%)[b]	3.4
Ramachandran outliers (%)[b]	0
Rotamer outliers (%)[b]	1.4
Clashscore[b]	2.51

Highest-resolution shell is shown in parentheses.
[a]R_{merge} = Σhkl |I(hkl) – < I(hkl) > |/ Σhkl(hkl), where < I(hkl) > is the mean of the symmetry equivalent reflections of I(hkl).
[b]As defined in MolProbity

molecular details responsible for biased signaling are unknown, recent crystallographic studies of G-protein-bound receptors (Carpenter et al., 2016; Rasmussen et al., 2011b), β-arrestin-bound Rhodopsin (Kang et al., 2015), the β-arrestin biased state of 5-HT_{2B}R (Wacker et al., 2013), as well as structure-inspired functional studies (Wootten et al., 2016) are beginning to clarify the essential structural features responsible for such signaling. Given the historical and continuing impact of LSD as a recreational drug, we wished to investigate the molecular mechanisms responsible for LSD's activity at serotonin receptors. We thus set out to (1) elucidate the structural characteristics of LSD-bound 5-HT_{2B}R, an excellent model system for 5-HT_{2A}R, (2) provide a detailed functional characterization of LSD's biased signaling profile, and (3) using the 5-HT_{2B}R structure as a template, clarify the structural features for its activity at the homologous 5-HT_{2A}R, the major target for LSD's psychedelic effects.

RESULTS

Insights from 5-HT_{2B}R/LSD Structure

To obtain structural insights into LSD's actions at human serotonin receptors, we crystallized an engineered 5-HT_{2B}R construct bound to LSD by extensively modifying our previous approach (Wacker et al., 2013). We eventually obtained crystals and solved the X-ray structure of the 5-HT_{2B}R/LSD complex to a resolution of 2.9 Å (Table 1; Figures 1 and S1). LSD is bound in the orthosteric binding site while also engaging the previously described extended binding site of the receptor (Figures 1A–1C) (Wang et al., 2013). As an ergoline, LSD's tryptamine moiety, which resembles that of 5-HT, is embedded in a tetracyclic scaffold (Figure 1D). Ergolines exhibit diverse amide modifications, such as LSD's diethylamide that is essential for its optimal potency in vivo (Nichols et al., 1996), or the peptide moiety of ergotamine (ERG) (Figure 1D). LSD is anchored to 5-HT_{2B}R by a conserved salt bridge between D135$^{3.32}$ in helix III and the basic nitrogen of the ergoline system (Figures 1B–1D), an interaction that has been observed consistently in aminergic receptor structures (Chien et al., 2010; Shimamura et al., 2011; Wacker et al., 2010, 2013; Wang et al., 2013). The ergoline system of LSD occupies the orthosteric pocket, which forms a narrow cleft lined mainly by hydrophobic side chains from residues in helices III, V, VI, and VII; such a cleft is common to most biogenic amine receptors. LSD's ergoline ring system forms edge-to-face aromatic contacts with conserved phenylalanines (F340$^{6.51}$, F341$^{6.52}$) in helix VI, as previously anticipated for its complex with 5-HT_{2A}R (Choudhary et al., 1995; Perez-Aguilar et al., 2014), and hydrogen bonds with the backbone of G221$^{5.42}$ in helix V. LSD's diethylamide group binds in a crevice between helices II, III, and VII, where one ethyl group forms non-polar contacts with L132$^{3.29}$ and W131$^{3.28}$, while the other ethyl group extends toward L362$^{7.35}$—residues previously shown to be part of an extended binding pocket in 5-HT_{1B} and 5-HT_{2B} receptors (Wacker et al., 2013; Wang et al., 2013) (Figure 1C).

LSD's Distinct Binding Pose

Although ergolines are structurally and chemically related, in vivo activities of ergolines are diverse, ranging from the anti-migraine effects of ERG to the hallucinogenic actions of LSD. These differences can be attributed in part to differential blood-brain barrier permeability—ERG, for example, does not cross the blood-brain barrier and is thus not hallucinogenic (Verhoeff et al., 1993). It is also known, however, that ergolines differ greatly in their

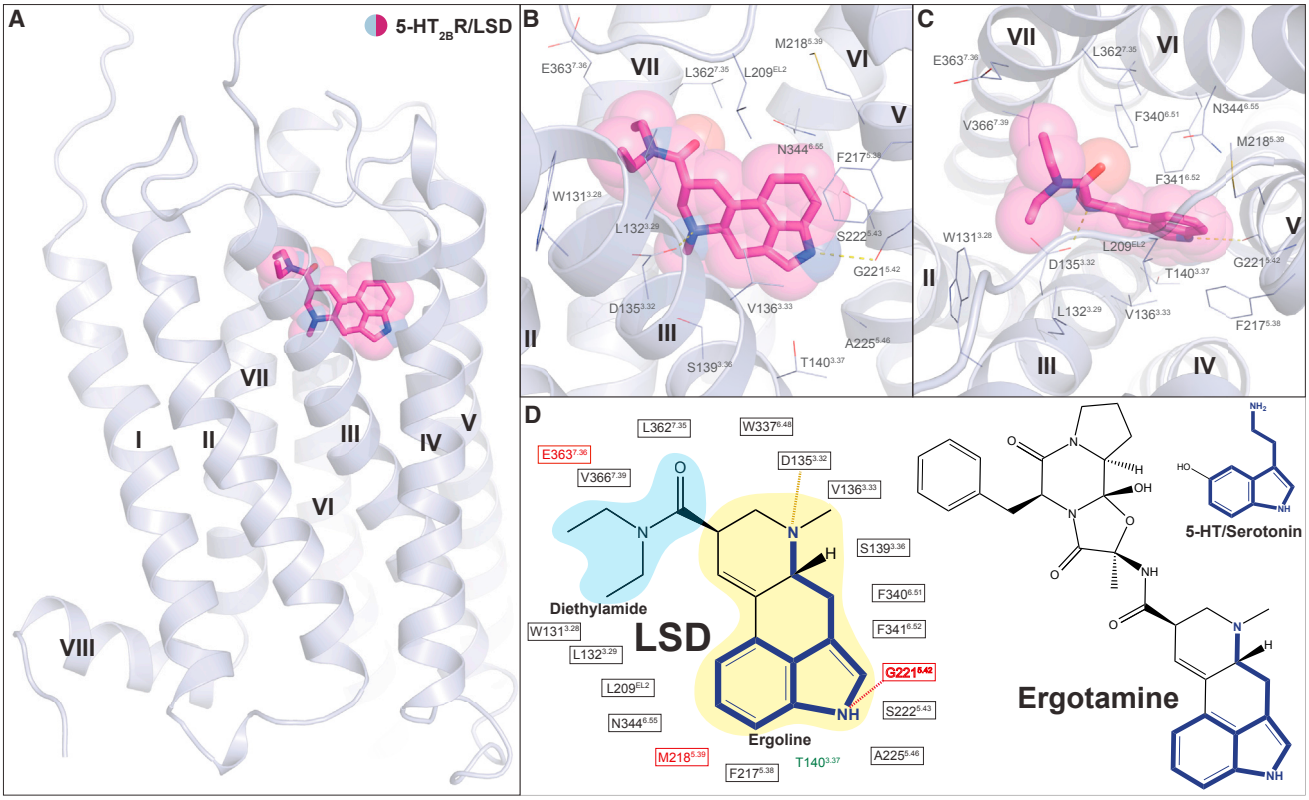

Figure 1. Architecture and Ligand-Receptor Interactions of the LSD-Bound Human 5-HT$_{2B}$ Receptor

(A) 5-HT$_{2B}$R cartoon representation (light blue) with helices labeled according to GPCR nomenclature. LSD is shown as a stick model with carbons, nitrogens, and oxygens colored in magenta, blue, and red, respectively. The LSD stick model is overlaid with a semi-transparent surface representation of the compound.

(B) Close-up view of LSD and the orthosteric binding site of the receptor from the membrane.

(C) Close-up view of LSD and the orthosteric binding site of the receptor from the extracellular space.

(D) 2D representation of LSD, Ergotamine (ERG), and 5-hydroxytryptamine (5-HT/serotonin). LSD belongs to the class of ergolines like ERG and contains a diethylamide substituent (highlighted in light blue) connected to the ergoline scaffold (highlighted in yellow). Ergolines contain a tryptamine core scaffold (dark blue) like the endogenous ligand 5-hydroxytryptamine (5-HT/serotonin). Diagram of interactions between LSD and the receptor in the ligand binding pocket is shown, with the hydrogen bonds between D135$^{3.32}$ and the LSD basic nitrogen in yellow, and G221$^{5.42}$ and the LSD indole nitrogen indicated by red dashes, respectively. Residues are labeled according to Ballesteros-Weinstein nomenclature. Residues highlighted in red show significant changes between LSD- and ERG-occupied 5-HT$_{2B}$R, while residues highlighted in green show a significant interaction with ERG but not LSD.

See also Figure S1.

receptor pharmacology and patterns of signaling (Huang et al., 2009). Ergolines are also predicted to bind to serotonin receptors differently based on modeling and site-directed mutagenesis studies (Choudhary et al., 1995). To investigate this possibility, we compared the conformations of 5-HT$_{2B}$R bound to either ERG or LSD (Figures 2 and S2). The 5-HT$_{2B}$R/LSD structure shows hallmarks of an apparently arrestin-biased state similar to those previously described for 5-HT$_{2B}$R/ERG, which include a partially activated state of the PIF motif, and larger activation-related changes in helix VII and the NPxxY motif than in helix V, VI, and the DRY motif (Wacker et al., 2013) (Figure S2). These similarities likely reflect the fact that at 5-HT$_{2B}$R, both ERG and LSD preferentially engage β-arrestin-mediated over Gq-mediated signal transduction (Wacker et al., 2013). Although LSD-bound 5-HT$_{2B}$R adopts an overall conformation reminiscent of that seen in the ERG-bound 5-HT$_{2B}$R structure, the shared ergoline ring systems of LSD and ERG adopt distinct configurations with respect to the orthosteric binding pocket of the 5-HT$_{2B}$R (Figure 2A).

Compared to ERG, the ergoline moiety of LSD is located higher in the orthosteric pocket, closer to EL2 and the extracellular space, adopting a shallow binding mode. ERG is located deeper in the pocket with its indole nitrogen hydrogen bonding to T140$^{3.37}$ in helix III, at the bottom of the pocket, further embedded in the intra-membrane region. In contrast, the indole nitrogen of LSD does not interact with T140$^{3.37}$ in helix III, but instead hydrogen bonds with the backbone oxygen of G221$^{5.42}$ in helix V.

We also observe conformational changes in the side chains of several important orthosteric pocket residues when comparing the structures of the LSD- and ERG-bound 5-HT$_{2B}$R: T114$^{2.64}$, E363$^{7.36}$, and M218$^{5.39}$ all change their rotamer states between the two structures (Figure 2A). These changes in rotamer states likely reflect distinct ligand-receptor interactions and an unexpected plasticity of the receptor for these structurally related compounds. For instance, in the 5-HT$_{2B}$R/ERG complex, the phenyl moiety of ERG appears to "push" down on M218$^{5.39}$, wedging the M218$^{5.39}$ side chain between the peptide and

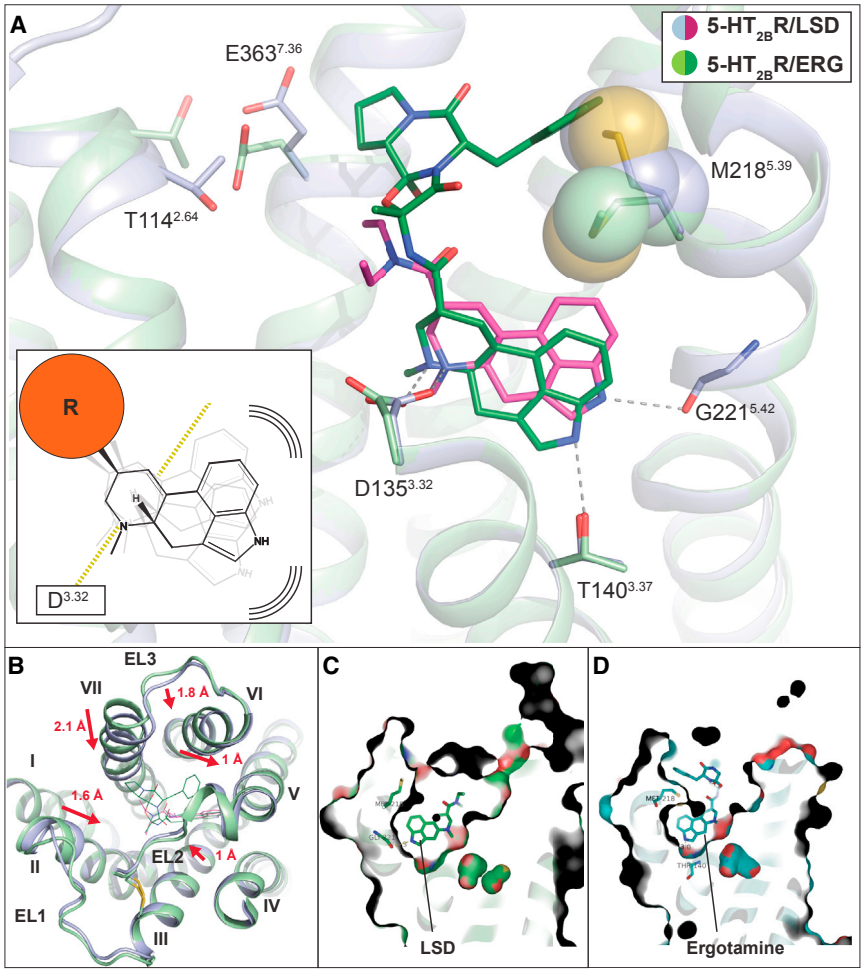

Figure 2. Conformational Differences in the Ligand Binding Pockets of LSD- and ERG-Bound 5-HT$_{2B}$R

(A) Close-up view of the orthosteric pockets of 5-HT$_{2B}$R (light blue) bound to LSD (magenta) superposed with 5-HT$_{2B}$R (green) bound to ERG (dark green). Compounds and relevant side chains are shown as sticks and residues are labeled according to Ballesteros-Weinstein nomenclature. Surface representation of M218$^{5.39}$ illustrates how ERG binding requires a conformational change to accommodate the phenyl ring of ERG. Insert shows schematic illustrating that different ergoline substituents (R, red circle) and their interactions with the receptor likely determine the orientation of the ergoline scaffold, which seems to be able to rotate around the hydrogen bond to the conserved aspartate D$^{3.32}$.

(B) View of the 5-HT$_{2B}$R ligand binding pocket from the extracellular space highlighting conformational differences in helix and loop positions in response to binding of ERG (green) versus LSD (light blue). Distances were measured between the Cα atoms of T114$^{2.64}$, L209^{EL2}, L347$^{6.58}$, N354^{EL3}, and T356$^{7.29}$.

(C and D) Surface representation illustrating shape of orthosteric binding pocket in the 5-HT$_{2B}$R/LSD complex (C) and the 5-HT$_{2B}$R/ERG complex (D). This particular cross-section cuts through M218$^{5.39}$ in such a way that the extended binding site appears smaller in the presence of ERG than in the presence of LSD, although calculation of binding pocket volume with CASTp shows a 28.6% decrease in overall volume of LSD versus ERG.

See also Figures S2 and S3.

ergoline moiety of ERG (Figure 2A) and thus contributing to the deeper seating of the ergoline moiety of ERG in the pocket versus that of LSD. In the 5-HT$_{2B}$R/LSD complex, by contrast, the diethylamide ergoline substituent does not interact with M218$^{5.39}$. As a result the M218$^{5.39}$ side chain flips up, allowing more space for LSD to adopt a shallower binding mode. We also examined these differential binding modes by molecular dynamics (MD) simulations, which provided additional support for the hypothesis that the binding of LSD preserves the unliganded conformation of M218$^{5.39}$, whereas binding of ERG distorts it. In MD simulations initiated from structures of either the ERG-bound or LSD-bound 5-HT$_{2B}$R but with the ligand removed, the M218$^{5.39}$ side chain consistently adopted an upward conformation matching that of the LSD-bound structure (Figure S3A). We performed over 100 μs of simulation (Table S1).

The smaller amide substituent of LSD also accounts for an overall contraction of the extended binding site relative to the ERG-bound structure (Figure 2B). Specifically, we observe an inward movement of helices II (1.6 Å), VII (2.1 Å), and parts of EL2 (1.0 Å) and EL3 (1.8 Å) toward the seven transmembrane core, and a relocation of helix VI (1.0 Å) away from helix VII toward helix V and the membrane, which is likely a result of the inward movement of helix VII (Figure 2B). Indeed, when we calculated the size of the binding pockets in the 5-HT$_{2B}$R/LSD and 5-HT$_{2B}$R/ERG complexes with CASTp (Dundas et al., 2006), we saw an overall reduction of the binding pocket volume from 2898.7 to 2068.4 Å^3—a 28.6% decrease. Together, these data illustrate how distinct but similar compounds—in this case LSD and ERG—differentially and unexpectedly shape the ligand binding surface of a GPCR (i.e., 5-HT$_{2B}$R; Figures 2C, 2D, S3C, and S3D). We also observed that the amide substituents of LSD and ERG are differentially arranged with respect to the ionic bond with D135$^{3.32}$ (Figure 2A, inset).

These observed rotamer changes and helical movements, as well as the differential positioning of the ergoline moiety, represent substantial structural changes that could reflect different receptor conformational and dynamic states. That is particularly evident when similar comparisons are made to the activation-related changes in the ligand-binding pocket of the β$_2$ adrenergic receptor (β$_2$AR); for β$_2$AR, a comparison of the antagonist-bound inactive state to the agonist-bound active state shows conformational changes of magnitude similar to those observed in the ligand-binding pocket of the ERG- versus LSD-bound 5-HT$_{2B}$R structures (Figures S3E–S3G). To quantify this, we calculated a ligand-binding pocket root-mean-square deviation (RMSD) of 0.99 Å for the ERG-bound versus LSD-bound

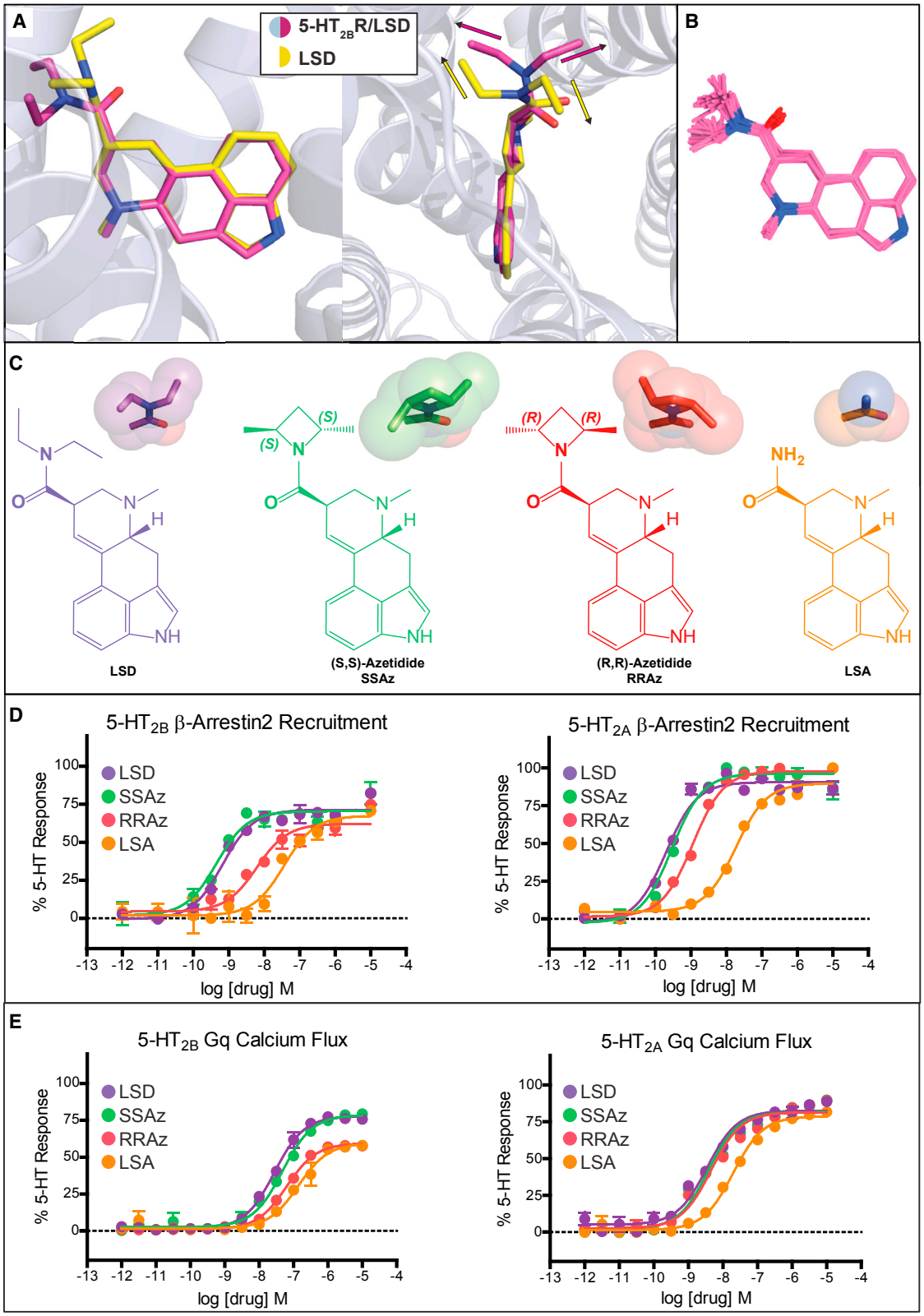

(legend on next page)

5-HT_{2B}R structures and an RMSD of 0.85 Å for the inactive- versus active-state structures of β_2AR.

LSD Diethylamide Stereoselectivity and Function

These structural rearrangements suggested to us that LSD's positioning in the binding pocket—mediated by the amide substituent—might be important for its signaling. The conformation of LSD in the 5-HT_{2B}R-bound crystal structure differs from the conformation in a receptor-free small-molecule crystal structure (Baker et al., 1972) by a ~60° rotation of the diethylamide moiety around the bond connecting it to the ergoline ring system (Figure 3A). Thus, although the two ethyl groups adopt a *trans* conformation in both crystal structures, their spatial positions relative to the ergoline ring system differ substantially. We initially explored the conformations of the ethyl groups computationally by MD. In MD simulations of the LSD-bound 5-HT_{2B}R, LSD maintained its receptor-bound crystallographic conformation, apart from fluctuations in the terminal methyl groups; we particularly note that LSD never visited the conformation it adopts in the small-molecule crystal structure (Figure 3B).

These findings suggested to us that the different conformations of the diethylamide moiety also might differentially stabilize receptor conformations and so be critical for receptor function. Accordingly, we employed sterically constrained LSD analogs (Figure 3C) (Nichols et al., 2002) to investigate the functional significance of different diethyl conformations. (*S*,*S*)-Azetidide (SSAz) and (*R*,*R*)-Azetidide (RRAz) are LSD analogs with constrained diethylamide conformations (Figure 3C). The SSAz conformation more closely resembles the diethyl conformation observed in the 5-HT_{2B}R bound LSD conformation, whereas RRAz is more similar to the diethyl conformation observed in the small molecule LSD crystal structure. This observation predicts that SSAz would more faithfully replicate the functional properties of LSD. To test this hypothesis, we performed functional assays at 5-HT_{2B}R and 5-HT_{2A}R, the presumed target of LSD's hallucinogenic actions. We found that although SSAz and LSD have nearly identical efficacies and potencies, RRAz and the unsubstituted ergoline lysergamide (LSA) have much reduced potencies for β-arrestin2 recruitment (Figure 3D). We also quantified Gq-mediated calcium flux and found the differences to be smaller (Figure 3E). The observation that the SSAz diethyl conformation matches LSD's functional preference is consistent with the particular conformation observed in the LSD-bound 5-HT_{2B}R crystal structure.

To investigate further the role of these ergoline substituents, we built a homology model of 5-HT_{2A}R based on our 5-HT_{2B}R/LSD crystal structure and docked LSD, SSAz, RRAz, and LSA into the binding pockets of both the 5-HT_{2B}R and 5-HT_{2A}R models (Figure S4; Table S2). The docked poses illustrate that LSD's crystallographic 5-HT_{2B}R binding mode is recapitulated in the 5-HT_{2A}R model and show that the rigidified substituent of SSAz adopts an almost identical orientation to that of LSD in its receptor bound forms (Figures S4A, S4B, S4E, and S4F). In contrast, the amide substituent of RRAz adopts a different orientation, with one of the ethyl groups pointing into solvent and not engaging in hydrophobic contacts with the receptor (Figures S4C and S4G), similar to LSA (Figures S4D and S4H). In combination, the structural and functional data together with MD simulations and docking studies support the hypothesis proposed some years ago (Nichols et al., 1996, 2002) that this conformation of the diethylamide moiety is key to LSD's potency and activity at 5-HT receptors.

A Structural Motif Associated with LSD Residence Time and Arrestin Translocation

Early radioligand binding studies using crude brain membrane preparations and [^{3}H]-LSD showed that LSD dissociated slowly from what were then ill-defined molecular targets (Bennett and Snyder, 1975). Here, we directly measured the off rate of [^{3}H]-LSD at 5-HT_{2B}R to obtain molecular insight into LSD's binding kinetics, as ligand residence times can profoundly modulate drug actions (Copeland et al., 2006). We found that LSD has a dissociation $t_{1/2}$ >5 hr at the 5-HT_{2B}R at 25°C (Figure S5A); even at 37°C, LSD exhibits a very slow dissociation rate with a residence time of ~46 min (k_{off} = 0.022 ± 0.004 min^{-1}; Figure 4A). Similarly, slow rates of [^{3}H]-LSD dissociation for 5-HT_{2B}R were seen with the crystallization construct expressed in Sf9 cells (Figure S5D) and in cells in which Gq and G_{11} proteins, or β-arrestins 1 and 2 were deleted (Figure S5E).

We noticed that in the LSD-bound 5-HT_{2B}R structure, residues 207–214 of EL2 form a "lid" over LSD (Figure 4B), likely hindering LSD's escape from the binding site and thus contributing to its slow dissociation rate. Indeed, a comparison of the 5-HT_{2B}R/LSD and 5-HT_{2B}R/ERG structures (Figures S3C and S3D) disclosed 5-HT_{2B}R/ERG to be more open. To test the hypothesis of a "lid" in the LSD structure responsible for its slow dissociation, we first performed MD simulations of both LSD-bound and unliganded 5-HT_{2B}R. We observed that the lid occasionally, although rarely, adopted a conformation in which the binding pocket was more exposed to the extracellular solvent (Figure 4B). We hypothesize that fluctuations in the position of the lid may be necessary for LSD to exit or enter the binding pocket, although the timescales of our simulations are far shorter than those on which LSD dissociates.

Figure 3. Diethylamide Configuration Determines LSD Pharmacology at 5-HT_{2B}R and 5-HT_{2A}R

(A) Side and top view of LSD (magenta)-bound 5-HT_{2B}R (light blue) crystal structure overlaid with small molecule crystal structure of unbound LSD (yellow) highlight differences in LSD's diethylamide conformation.

(B) Snapshots of LSD (magenta) from a 5-HT_{2B}R-bound MD simulation show that LSD maintains its 5-HT_{2B}R-bound crystallographic conformation, with substantial fluctuation only in the terminal methyl groups. Snapshots are aligned on the ergoline ring system.

(C) Chemical structures of LSD (purple) and diethyl constrained lysergamides, (*S*,*S*)-Azetidide (SSAz, green), (*R*,*R*)-Azetidide (RRAz, red), and lysergic acid amide (LSA, orange) indicating 5-HT_{2B}R-bound LSD diethyl conformation resembles the conformation of (*S*,*S*)-Azetidide.

(D) Lysergamide-mediated β-arrestin2 recruitment at 5-HT_{2B}R and 5-HT_{2A}R (n = 3) highlights the importance of diethylamide conformation for LSD's function.

(E) Lysergamide-mediated Gq-calcium flux at 5-HT_{2B}R and 5-HT_{2A}R (n = 3) indicates lack of stereospecific preference for LSD azetidides in this pathway.

See also Figure S4 and Table S2.

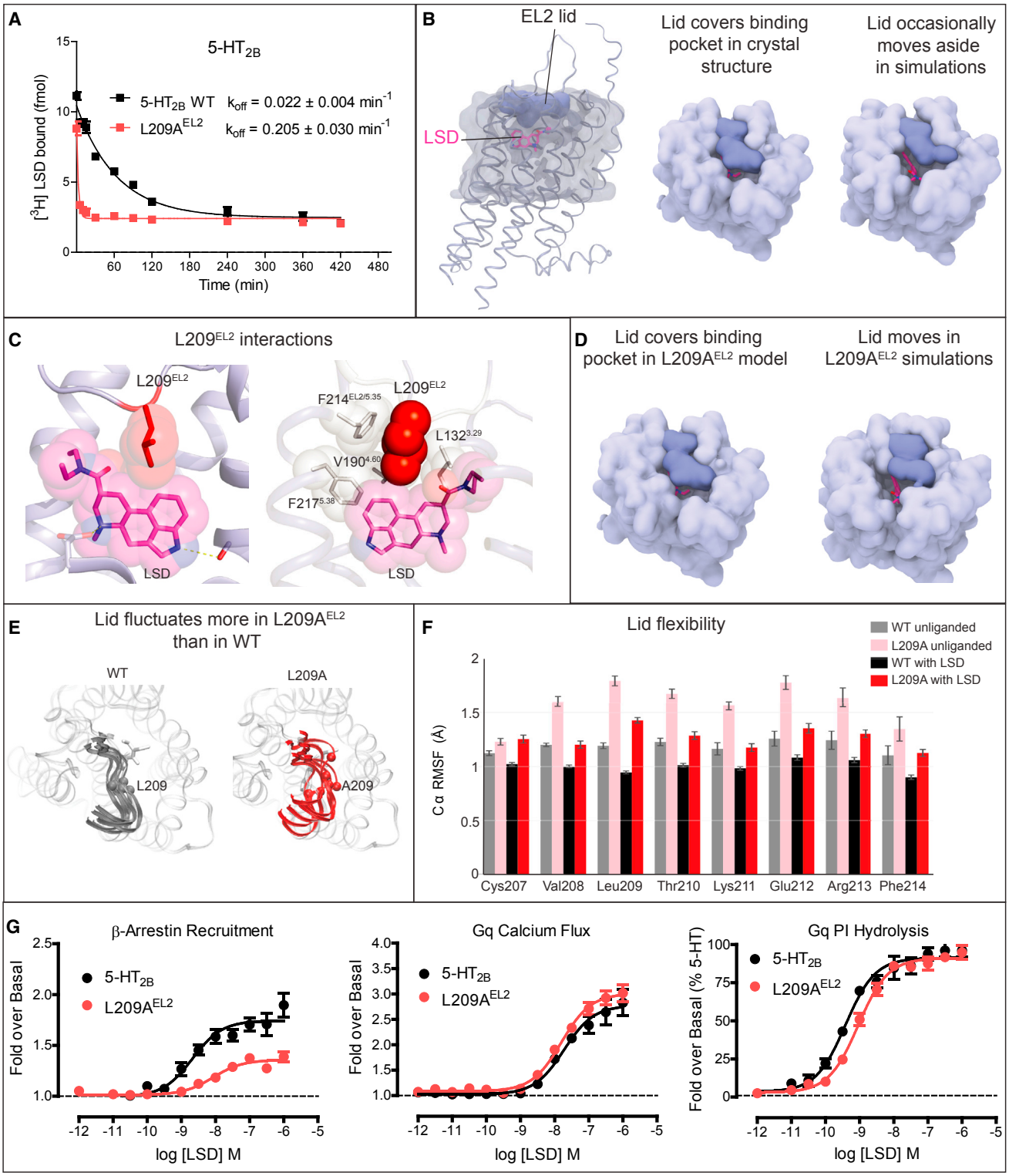

Figure 4. Mutation of an EL2 "Lid" Decreases LSD's Long Residence Time at 5-HT$_{2B}$R, which Affects Functional Selectivity

(A) Comparison of LSD dissociation from wild-type 5-HT$_{2B}$R and L209A^{EL2} mutant (n = 3) at 37°C shows a slow LSD off-rate at the wild-type and a faster off-rate at the mutant.

(B) (left and center) In the 5-HT$_{2B}$R crystal structure, EL2 residues 207–214 form a lid (dark blue, with other nearby residues in light blue) that covers the binding pocket. (right) In MD simulations of the wild-type, this lid occludes access to the binding pocket most of the time, but occasionally moves aside.

(legend continued on next page)

Table 2. LSD Dissociation and Association Rates at Wild-Type and Mutant 5-HT_{2A}R and 5-HT_{2B}R

Receptor	B_{MAX} ± SEM fmol/mg protein	Residence Time, min (k_{off} ± SEM) min^{-1}	k_{on} ± SEM, M^{-1} min^{-1}	K_d, nM (pKd ± SEM)
5-HT_{2A}R wild-type	2,180 ± 350	221 (0.005 ± 0.001)	$1.58 \times 10^7 \pm 4.06 \times 10^6$	0.33 (9.48 ± 0.11)
5-HT_{2A}R L229A^{EL2}	1,650 ± 520	50 (0.020 ± 0.003)	$3.34 \times 10^7 \pm 6.20 \times 10^6$	0.81 (9.22 ± 0.25)
5-HT_{2B}R wild-type	3,010 ± 614	46 (0.022 ± 0.004)	$2.59 \times 10^7 \pm 3.04 \times 10^6$	0.91 (9.08 ± 0.09)
5-HT_{2B}R L209A^{EL2}	3,628 ± 598	4 (0.236 ± 0.033)	$4.20 \times 10^7 \pm 5.36 \times 10^6$	2.31 (8.63 ± 0.08)

Data were acquired by association and dissociation kinetic experiments conducted in parallel at 37°C using [^{3}H]LSD (concentration range 0.2–5.0 nM). Estimates of k_{off}, k_{on}, and K_d were obtained from three independent experiments performed in duplicate. Residence time was calculated as $1/k_{off}$.

In the LSD-bound crystal structure, the side chain of the lid residue L209^{EL2} forms extensive hydrophobic contacts with both LSD and surrounding residues in TMs III, IV, and V (Figure 4C). When the lid moved aside to expose the binding pocket in simulation, several of these contacts broke. We thus hypothesized that L209^{EL2} acts as a latch, reducing the mobility of the lid and constraining LSD's access to and egress from the binding pocket. Indeed, simulations of a receptor in which this latch was removed by mutating L209^{EL2} to alanine showed much increased lid fluctuations, both with and without LSD present (Figures 4D–4F and S3B). This model was further tested by creating the L209A^{EL2} mutant, which decreased LSD residence time by 10-fold, from 44 min to 4.3 min, at 37°C (Figure 4A; Table 2). The L209A^{EL2} mutation also accelerates LSD's apparent on-rate (Figure S5B; Table 2) without substantially altering [^{3}H]-LSD's steady-state binding affinity (Figure S5C). This effect was not seen with ERG as its binding kinetics are minimally affected by the L209A^{EL2} mutation (Figures S5F and S5G). This is perhaps due to the more extensive contacts between ERG and the receptor compared to LSD (Figure 2A), which are possibly responsible for the different EL2 conformations in the 5-HT_{2B}R/LSD and 5-HT_{2B}R/ERG structures (Figure 2B).

Although many studies demonstrate that drug residence time can correlate with drug efficacy in vivo (Copeland et al., 2006), it is possible that off-rate or residence time might also modulate kinetically sensitive patterns of intracellular signaling. To investigate this possibility, we assessed the functional consequence of LSD's long residence time on 5-HT_{2B}R signaling by characterizing apparent signaling profiles at the wild-type and L209A^{EL2} receptors. Comparing Gq-mediated calcium flux and β-arrestin2 recruitment, we find that the L209A^{EL2} mutation strongly and selectively reduces LSD's β-arrestin2 recruitment potency and efficacy without affecting Gq-mediated calcium flux or PI hydrolysis (Figure 4G; Table S3).

We wondered whether this model of LSD's actions at a molecular level held true for the 5-HT_{2A}R, which represents LSD's principal molecular target in vivo. As shown in Figure 5A, we observe a configuration of LSD docked in the binding pocket of the 5-HT_{2A}R model similar to that observed in the 5-HT_{2B}R/LSD crystal structure, with the conformation of EL2 and L229^{EL2} forming contacts with LSD similar to L209^{EL2} in the 5-HT_{2B}R/LSD crystal structure. Remarkably, [^{3}H]-LSD dissociation experiments reveal an even slower off rate (k_{off} = 0.005 ± 0.001 min^{-1}) and thus longer residence time of LSD at 5-HT_{2A}R compared to 5-HT_{2B}R. Importantly, the L229A^{EL2} mutation substantially decreases LSD's residence time from 221 min (5-HT_{2A}R wild-type) to 50 min (L229A^{EL2}) (Figure 5B; Table S4). Similar to the findings obtained for 5-HT_{2B}R, LSD also exhibits selectively reduced β-arrestin2 recruitment potency and efficacy at the 5-HT_{2A}R EL2 mutant L229A^{EL2} without altered Gq-mediated calcium flux (Figure 5C; Table S4).

To investigate the hypothesis that LSD's slow binding kinetics are important for its signaling and the kinetics of signaling, we next modified a bioluminescence resonance energy transfer (BRET) assay (Hamdan et al., 2005; Masri et al., 2008) for kinetic measurements of β-arrestin2 recruitment at 5-HT_{2A}R and 5-HT_{2B}R. Consistent with our hypothesis, both LSD-mediated β-arrestin2 recruitment and Gq-mediated signaling increase with prolonged compound incubation (Figures 5D, 5E, and S5F–S5I), an effect correlated with LSD's prolonged residence time at both receptors. We also tested LSD-mediated β-arrestin2 recruitment at the 5-HT_{2A}R L229A^{EL2} and 5-HT_{2B}R L209A^{EL2} mutants, which reduce LSD's residence time. Remarkably, LSD exhibits weak β-arrestin2 recruitment potency at both EL2 mutants and no time-dependent increase in LSD's potency is observed (Figures 5D and 5E). Although a similar time dependence of potency and efficacy was seen for Gq-mediated

(C) (left) LSD (magenta) bound to 5-HT_{2B}R (light blue) orthosteric pocket viewed from membrane and extracellular space, with EL2 residue L209^{EL2} highlighted in red. (right) The L209^{EL2} side chain (now viewed from roughly the opposite direction) forms extensive hydrophobic contacts with residues in TMs III, IV, and V.
(D) Mutating L209^{EL2} to alanine does not lead to a more exposed binding pocket in the crystal structure (left); exposure of the binding pocket still depends on motion of the lid, as seen in simulation (right).
(E) The lid is more mobile in simulations of the mutant (red) than in simulations of the wild-type (gray). Each image shows six representative snapshots of the lid from simulation, with the remainder of the receptor in light gray. The alpha carbon atom of residue 209 is shown as a sphere.
(F) Root-mean-square fluctuation (RMSF) of the alpha carbon of each lid residue provides a quantitative measure of mobility, demonstrating that the lid fluctuates more in simulations of the L209A^{EL2} mutant than in simulations of the wild-type receptor, whether or not LSD is bound. RMSF measures the fluctuations of an atom around its average position during simulation. Error bars show SEM across three to nine simulations per condition. Replace this sentence by Differences in RMSFs between wild-type and mutant LSD-bound simulations (black vs. red bars) are significant for all residues shown ($p < 0.01$, as measured by a two-sided Welch's t test). Differences in RMSFs between wild-type and mutant unliganded simulations (gray vs. pink bars) are significant ($p < 0.01$) for all residues shown except Cys207 and Phe214.
(G) Arrestin and Gq functional activities indicate that 5-HT_{2B}R L209A^{EL2} mutant selectivity disrupts β-arrestin2 recruitment activity, leaving Gq function intact (n = 3).
See also Figures S3 and S5 and Tables S1, S3, and S4.

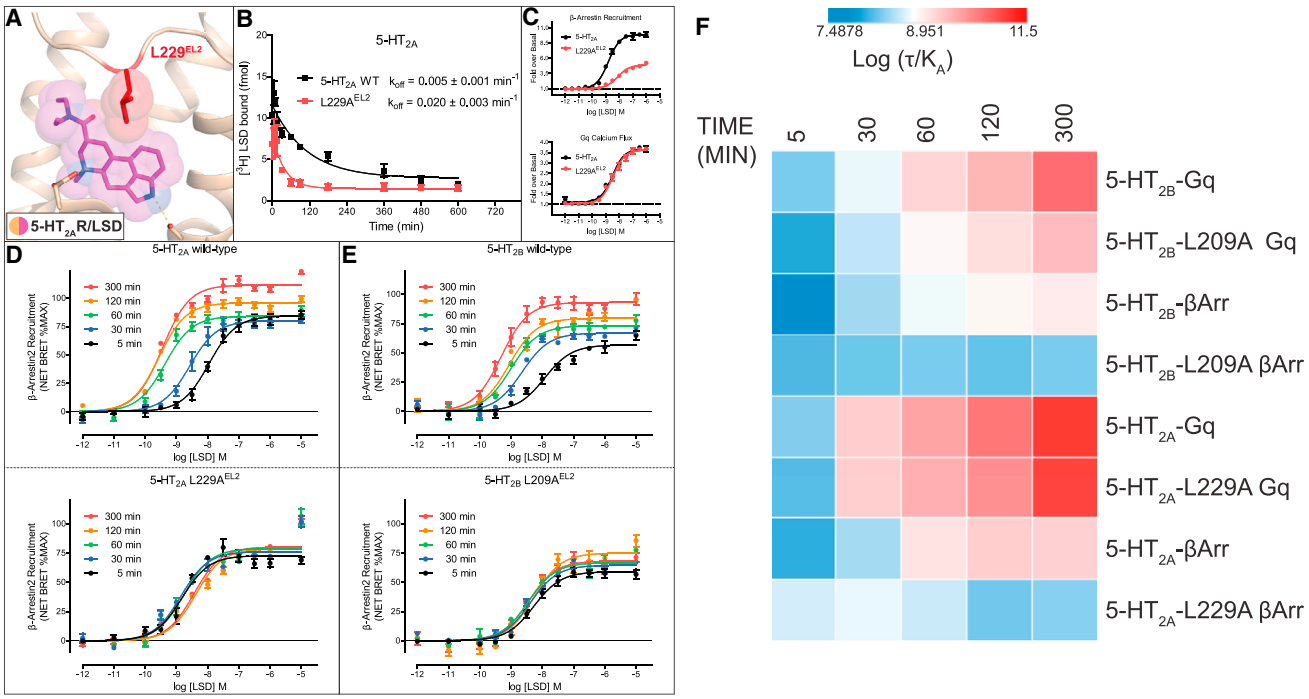

Figure 5. Accelerated Ligand Kinetics Also Affect Pharmacological Profile of LSD at 5-HT$_{2A}$R

(A) Docking pose of LSD (magenta) in 5-HT$_{2A}$R model (beige) illustrates similar binding mode compared to 5-HT$_{2B}$R/LSD complex structure. L229^{EL2} (red) is in the same position as L209^{EL2} in the 5-HT$_{2B}$R/LSD complex structure.

(B) Comparison of LSD dissociation from wild-type 5-HT$_{2A}$R and L229A^{EL2} mutant (n = 3), shows increased LSD off-rate at the mutant receptor.

(C) Arrestin and Gq functional activities indicate that 5-HT$_{2A}$R L229A^{EL2} mutant selectivity disrupts β-arrestin2 recruitment activity, leaving Gq function intact (n = 3).

(D) Kinetic measurement of LSD-mediated β-arrestin2 recruitment at wild-type 5-HT$_{2A}$R and L229A^{EL2} mutant using bioluminescence resonance energy transfer (BRET). At the wild-type receptor, LSD's potency and efficacy increase with longer compound stimulation, whereas LSD exhibits weak potency and efficacy at the L229A^{EL2} mutant that does not change over time.

(E) Kinetic measurement of LSD-mediated β-arrestin2 recruitment at wild-type 5-HT$_{2B}$R and the L209A^{EL2} mutant using bioluminescence resonance energy transfer (BRET). At the wild-type receptor, LSD's potency and efficacy increase with longer compound stimulation, whereas LSD exhibits weak potency and efficacy at the L209A^{EL2} mutant that does not change over time.

(F) Heatmap of time-dependent alterations in signaling for WT and mutant 5-HT$_{2A}$R and 5-HT$_{2B}$R. The heatmap (see STAR Methods for details) illustrates how signaling as quantified by calculating transduction coefficients are altered in a time-dependent fashion at WT and mutant 5-HT$_{2A}$R and 5-HT$_{2B}$R. Time is measured in minutes.

See also Figure S5 and Tables S4 and S5.

inositol phosphates (IP) accumulation, we observed no substantial effect of the EL2 mutation on the time-dependent augmentation of Gq signaling (Figures S5F–S5I).

To obtain a global view of the role of kinetics for LSD's actions at 5-HT$_{2A}$R and 5-HT$_{2B}$R—particularly with regard to L229^{EL2} and L209^{EL2}, respectively—we provide a heatmap plot of transduction coefficients [i.e., log (τ/K$_A$); (Kenakin et al., 2012)] of the time-course data for Gq (IP accumulation) and arrestin translocation (Figure 5F; Table S5). As can be seen for Gq-mediated IP accumulation and β-arrestin2 recruitment, time-dependent augmentation of the transduction coefficient is evident. Remarkably, the L209A^{EL2} and L229A^{EL2} mutations selectively abrogate the time-dependency for β-arrestin2 translocation.

DISCUSSION

A molecular understanding of the structural basis of psychoactive drug action has long been elusive. LSD, with its profound activity on human perception and awareness, is one of the most prominent psychoactive drugs. Whereas it has long been thought that LSD and many other hallucinogens act at serotonin receptors (Shaw and Woolley, 1956; Vane, 1957; Woolley and Shaw, 1954), understanding LSD's actions at a molecular level has remained clouded, notwithstanding important computational (Perez-Aguilar et al., 2014), genetic, behavioral, and pharmacological studies (González-Maeso et al., 2007). The structure of LSD bound to one of its molecular targets, and the signaling and simulation studies it enables, begins to address long-standing questions about the relation of LSD's chemical structure to its activity, kinetics, and signaling. Two noteworthy observations stand out. First, the key amide side chain of LSD—the group that distinguishes it from the far less hallucinogenic lysergamide (LSA)—adopts a constrained conformation in the binding site that cannot exchange readily with alternative conformational states. This conformation, and by extension the contacts made, is crucial for LSD's actions, and close analogs

that cannot adopt it are much less active in vivo. Second, this conformation apparently contributes to LSD's relatively potent ability to promote β-arrestin translocation.

The structure of the 5-HT_{2B}R/LSD complex reveals that the amide substituents, such as LSD's diethylamide, largely determine the positioning of the ergoline system within the orthosteric pocket. This new structure explains the previously enigmatic requirement of LSD and related lysergamides for a specific conformation of the diethylamide substituents for activity. The observation that, for instance, the probe molecule SSAz is active, whereas its stereoisomer RRAz is less active (Nichols et al., 2002) was difficult to reconcile with the prior small molecule crystal structure of LSD alone (Baker et al., 1972), in which the diethylamide adopts a different conformation. As the receptor-LSD complex structure shows, the diethylamide of receptor-bound LSD adopts a conformation consistent with the observed stereochemical preference for SSAz over RRAz at both the 5-HT_{2A} and 5-HT_{2B} receptors.

The diethylamide positioning and interactions could also contribute to LSD's long residence time at 5-HT_{2B}R and 5-HT_{2A}R—its presumed major molecular target. MD simulations suggest the slow kinetics of LSD are due, at least in part, to a lid formed by EL2 covering the binding pocket. Compellingly, accelerating LSD's binding kinetics by making a substitution to a key residue identified structurally ($L209^{EL2}$), selectively attenuates the time-dependent augmentation of β-arrestin2 recruitment while minimally affecting Gq signaling. We note in this regard that, although structural studies cannot provide definitive insights into drug actions in vivo, it is conceivable that LSD's long residence time via EL2 interactions could contribute to LSD's long duration of action (Schmid et al., 2015), despite its apparent rapid clearance from the body [$t_{1/2}$ = 3.6 hr (Dolder et al., 2015)].

Crystal structures and molecular simulations can never fully explain CNS drug efficacy, which for LSD requires integrative action over complex neural networks, leading to highly distinctive cognitive effects. Our observations nevertheless provide the first structure-informed insights into the molecular actions for any hallucinogen. Our findings explain the role of LSD functional groups whose importance in vivo has long been recognized, but whose mechanism has been opaque. The structure-informed insights also link these particular interactions to the unusual signaling kinetics of LSD—particularly as it relates to β-arrestin translocation, effects that could be crucial for its hallucinogenic activity in vivo (W.C. Wetsel, R.M. Rodriguez, and B.L.R., unpublished data). Finally, this structure may template future structure-based efforts to discover new chemotypes at 5-HT_{2A} and 5-HT_{2B} receptors. Such molecules could help disentangle hallucinogenic effects from other intriguing activities of 5-HT_{2A} agonists, something that has heretofore been impossible but that a structure-based approach, with its ability to identify novel chemotypes, now allows (Huang et al., 2015; Manglik et al., 2016).

STAR★METHODS

Detailed methods are provided in the online version of this paper and include the following:

- KEY RESOURCES TABLE
- CONTACT FOR REAGENT AND RESOURCE SHARING
- METHOD DETAILS
  - Generation of 5-HT_{2B}R receptor crystallization construct
  - Expression and purification of 5-HT_{2B}R
  - Lipidic cubic phase crystallization
  - Data collection, structure solution, and refinement
  - LSD synthesis
  - Calcium flux assay
  - Tango arrestin recruitment assay
  - Phosphoinositide hydrolysis assay
  - Bioluminescence resonance energy transfer arrestin assay
  - Ligand association and dissociation radioligand binding assays
  - MD simulations set-up
  - MD simulation force field parameters
  - MD simulation protocol
  - Analysis protocols for MD simulations
  - Homology modeling of 5-HT_{2A}R
  - Molecular docking of LSD and its derivatives
- QUANTIFICATION AND STATISTICAL ANALYSIS
  - Dose response, log(τ/K_A) calculation and ligand bias quantification
- DATA AND SOFTWARE AVAILABILITY
  - Data Resources

SUPPLEMENTAL INFORMATION

Supplemental Information includes five figures and five tables and can be found with this article online at http://dx.doi.org/10.1016/j.cell.2016.12.033.

An audio PaperClip is available at http://dx.doi.org/10.1016/j.cell.2016.12.033#mmc2.

AUTHOR CONTRIBUTIONS

D.W. designed experiments, was responsible for the overall crystallization and structure determination strategy, expressed the protein, purified the receptor, optimized crystallization conditions, grew crystals for data collection, collected and processed diffraction data, determined and analyzed the structure, and prepared the manuscript. S.W. expressed the protein, purified the receptor, optimized crystallization conditions, grew crystals for data collection, collected diffraction data, and assisted with preparing the manuscript. J.D.M. designed experiments, performed mutagenesis, ligand binding and signaling studies, analyzed the data, and prepared the manuscript. R.M.B. and A.J.V. performed and analyzed MD simulations and edited the manuscript. A.L. built the 5-HT_{2A}R homology model and performed the docking experiments and edited the manuscript. K.L. collected the IP accumulation data. Z.L.S. assisted with diffraction data collection, molecular biology, and radioligand binding assays. T.C. assisted with radioligand binding assays. D.E.N. synthesized LSD and LSD analogs, provided invaluable insights, and edited the paper. B.K.S. supervised the docking experiments and edited the manuscript. R.O.D. supervised the MD simulation studies, prepared parts of the manuscript, and edited the manuscript. B.L.R designed the experiments, was responsible for the overall project strategy and management, and prepared the manuscript.

ACKNOWLEDGMENTS

This work was supported by NIH grants RO1MH61887 and U19MH82441, the NIMH Psychoactive Drug Screening Program Contract (all to B.L.R.),

GM59957 (to B.K.S.), a Terman Faculty Fellowship (R.O.D.), and the Michael Hooker Distinguished Chair of Pharmacology (B.L.R.). The CRISPR-generated knockout HEK293 cells were a generous gift from A. Inoue (Tohoku University). We also gratefully acknowledge J. Sondek and S. Endo-Streeter for providing independent structure quality control analysis; M.J. Miley and the UNC macromolecular crystallization core for advice and use of their equipment for crystal harvesting and transport, which is supported by the National Cancer Institute under award number P30CA016086; J. Smith, R. Fischetti, and the staff of GM/CA@APS, which has been funded with federal funds from the National Cancer Institute (ACB-12002) and the National Institute of General Medical Sciences (AGM-12006). This research used resources of the Advanced Photon Source, a U.S. Department of Energy (DOE) Office of Science User Facility operated for the DOE Office of Science by Argonne National Laboratory under contract no. DE-AC02-06CH11357.

Received: August 10, 2016
Revised: November 29, 2016
Accepted: December 21, 2016
Published: January 26, 2017

REFERENCES

Adams, P.D., Afonine, P.V., Bunkóczi, G., Chen, V.B., Davis, I.W., Echols, N., Headd, J.J., Hung, L.W., Kapral, G.J., Grosse-Kunstleve, R.W., et al. (2010). PHENIX: A comprehensive Python-based system for macromolecular structure solution. Acta Crystallogr. D Biol. Crystallogr. *66*, 213–221.

Allen, J.A., Yost, J.M., Setola, V., Chen, X., Sassano, M.F., Chen, M., Peterson, S., Yadav, P.N., Huang, X.P., Feng, B., et al. (2011). Discovery of β-arrestin-biased dopamine D2 ligands for probing signal transduction pathways essential for antipsychotic efficacy. Proc. Natl. Acad. Sci. USA *108*, 18488–18493.

Baker, R.W., Chothia, C., Pauling, P., and Weber, H.P. (1972). Molecular structure of LSD. Science *178*, 614–615.

Bennett, J.P., Jr., and Snyder, S.H. (1975). Stereospecific binding of D-lysergic acid diethylamide (LSD) to brain membranes: Relationship to serotonin receptors. Brain Res. *94*, 523–544.

Berger, M., Gray, J.A., and Roth, B.L. (2009). The expanded biology of serotonin. Annu. Rev. Med. *60*, 355–366.

Best, R.B., Mittal, J., Feig, M., and MacKerell, A.D., Jr. (2012a). Inclusion of many-body effects in the additive CHARMM protein CMAP potential results in enhanced cooperativity of α-helix and β-hairpin formation. Biophys. J. *103*, 1045–1051.

Best, R.B., Zhu, X., Shim, J., Lopes, P.E., Mittal, J., Feig, M., and Mackerell, A.D., Jr. (2012b). Optimization of the additive CHARMM all-atom protein force field targeting improved sampling of the backbone φ, ψ and side-chain χ(1) and χ(2) dihedral angles. J. Chem. Theory Comput. *8*, 3257–3273.

Black, J.W., and Leff, P. (1983). Operational models of pharmacological agonism. Proc. R. Soc. Lond. B Biol. Sci. *220*, 141–162.

Bogenschutz, M.P., and Johnson, M.W. (2016). Classic hallucinogens in the treatment of addictions. Prog. Neuropsychopharmacol. Biol. Psychiatry *64*, 250–258.

Bourdon, D.M., Wing, M.R., Edwards, E.B., Sondek, J., and Harden, T.K. (2006). Quantification of isozyme-specific activation of phospholipase C-beta2 by Rac GTPases and phospholipase C-epsilon by Rho GTPases in an intact cell assay system. Methods Enzymol. *406*, 489–499.

Caffrey, M., and Cherezov, V. (2009). Crystallizing membrane proteins using lipidic mesophases. Nat. Protoc. *4*, 706–731.

Carhart-Harris, R.L., Muthukumaraswamy, S., Roseman, L., Kaelen, M., Droog, W., Murphy, K., Tagliazucchi, E., Schenberg, E.E., Nest, T., Orban, C., et al. (2016). Neural correlates of the LSD experience revealed by multimodal neuroimaging. Proc. Natl. Acad. Sci. USA *113*, 4853–4858.

Carpenter, B., Nehmé, R., Warne, T., Leslie, A.G., and Tate, C.G. (2016). Structure of the adenosine A(2A) receptor bound to an engineered G protein. Nature *536*, 104–107.

Case, D.A., Berryman, J.T., Betz, R.M., Cerutti, D.S., and Cheatham, I. (2015). T.E., Darden, T.A., Duke, R.E., Giese, T.J., Gohlke, H., Goetz, A.W., *et al* (AMBER).

Chambers, C.C., Hawkins, G.D., Cramer, C.J., and Truhlar, D.G. (1996). Model for aqueous solvation based on class IV atomic charges and first solvation shell effects. J. Phys. Chem. *100*, 16385–16398.

Chien, E.Y., Liu, W., Zhao, Q., Katritch, V., Han, G.W., Hanson, M.A., Shi, L., Newman, A.H., Javitch, J.A., Cherezov, V., and Stevens, R.C. (2010). Structure of the human dopamine D3 receptor in complex with a D2/D3 selective antagonist. Science *330*, 1091–1095.

Choudhary, M.S., Sachs, N., Uluer, A., Glennon, R.A., Westkaemper, R.B., and Roth, B.L. (1995). Differential ergoline and ergopeptine binding to 5-hydroxytryptamine2A receptors: Ergolines require an aromatic residue at position 340 for high affinity binding. Mol. Pharmacol. *47*, 450–457.

Chu, R., Takei, J., Knowlton, J.R., Andrykovitch, M., Pei, W., Kajava, A.V., Steinbach, P.J., Ji, X., and Bai, Y. (2002). Redesign of a four-helix bundle protein by phage display coupled with proteolysis and structural characterization by NMR and X-ray crystallography. J. Mol. Biol. *323*, 253–262.

Chun, E., Thompson, A.A., Liu, W., Roth, C.B., Griffith, M.T., Katritch, V., Kunken, J., Xu, F., Cherezov, V., Hanson, M.A., and Stevens, R.C. (2012). Fusion partner toolchest for the stabilization and crystallization of G protein-coupled receptors. Structure *20*, 967–976.

Coleman, R.G., Carchia, M., Sterling, T., Irwin, J.J., and Shoichet, B.K. (2013). Ligand pose and orientational sampling in molecular docking. PLoS ONE *8*, e75992.

Copeland, R.A., Pompliano, D.L., and Meek, T.D. (2006). Drug-target residence time and its implications for lead optimization. Nat. Rev. Drug Discov. *5*, 730–739.

Dolder, P.C., Schmid, Y., Haschke, M., Rentsch, K.M., and Liechti, M.E. (2015). Pharmacokinetics and concentration-effect relationship of oral LSD in humans. Int. J. Neuropsychopharmacol. *19*, 19.

Dundas, J., Ouyang, Z., Tseng, J., Binkowski, A., Turpaz, Y., and Liang, J. (2006). CASTp: Computed atlas of surface topography of proteins with structural and topographical mapping of functionally annotated residues. Nucleic Acids Res. *34*, W116-8.

Emsley, P., Lohkamp, B., Scott, W.G., and Cowtan, K. (2010). Features and development of Coot. Acta Crystallogr. D Biol. Crystallogr. *66*, 486–501.

Gallagher, K., and Sharp, K. (1998). Electrostatic contributions to heat capacity changes of DNA-ligand binding. Biophys. J. *75*, 769–776.

Gasser, P., Kirchner, K., and Passie, T. (2015). LSD-assisted psychotherapy for anxiety associated with a life-threatening disease: A qualitative study of acute and sustained subjective effects. J. Psychopharmacol. (Oxford) *29*, 57–68.

Ghanouni, P., Schambye, H., Seifert, R., Lee, T.W., Rasmussen, S.G., Gether, U., and Kobilka, B.K. (2000). The effect of pH on beta(2) adrenoceptor function. Evidence for protonation-dependent activation. J. Biol. Chem. *275*, 3121–3127.

González-Maeso, J., Weisstaub, N.V., Zhou, M., Chan, P., Ivic, L., Ang, R., Lira, A., Bradley-Moore, M., Ge, Y., Zhou, Q., et al. (2007). Hallucinogens recruit specific cortical 5-HT(2A) receptor-mediated signaling pathways to affect behavior. Neuron *53*, 439–452.

Hamdan, F.F., Audet, M., Garneau, P., Pelletier, J., and Bouvier, M. (2005). High-throughput screening of G protein-coupled receptor antagonists using a bioluminescence resonance energy transfer 1-based beta-arrestin2 recruitment assay. J. Biomol. Screen. *10*, 463–475.

Hanson, M.A., Brooun, A., Baker, K.A., Jaakola, V.P., Roth, C., Chien, E.Y., Alexandrov, A., Velasquez, J., Davis, L., Griffith, M., et al. (2007). Profiling of membrane protein variants in a baculovirus system by coupling cell-surface detection with small-scale parallel expression. Protein Expr. Purif. *56*, 85–92.

Hawkins, P.C., Skillman, A.G., Warren, G.L., Ellingson, B.A., and Stahl, M.T. (2010). Conformer generation with OMEGA: Algorithm and validation using high quality structures from the Protein Databank and Cambridge Structural Database. J. Chem. Inf. Model. *50*, 572–584.

Hofmann, A. (1979). How LSD originated. J. Psychedelic Drugs *11*, 53–60.

Hopkins, C.W., Le Grand, S., Walker, R.C., and Roitberg, A.E. (2015). Long-Time-Step Molecular Dynamics through Hydrogen Mass Repartitioning. J. Chem. Theory Comput. *11*, 1864–1874.

Huang, J., and MacKerell, A.D., Jr. (2013). CHARMM36 all-atom additive protein force field: Validation based on comparison to NMR data. J. Comput. Chem. *34*, 2135–2145.

Huang, X.P., Setola, V., Yadav, P.N., Allen, J.A., Rogan, S.C., Hanson, B.J., Revankar, C., Robers, M., Doucette, C., and Roth, B.L. (2009). Parallel functional activity profiling reveals valvulopathogens are potent 5-hydroxytryptamine(2B) receptor agonists: Implications for drug safety assessment. Mol. Pharmacol. *76*, 710–722.

Huang, X.P., Karpiak, J., Kroeze, W.K., Zhu, H., Chen, X., Moy, S.S., Saddoris, K.A., Nikolova, V.D., Farrell, M.S., Wang, S., et al. (2015). Allosteric ligands for the pharmacologically dark receptors GPR68 and GPR65. Nature *527*, 477–483.

Humphrey, W., Dalke, A., and Schulten, K. (1996). VMD: Visual molecular dynamics. J. Mol. Graph *14*, 33–38.

Jakab, R.L., and Goldman-Rakic, P.S. (1998). 5-Hydroxytryptamine2A serotonin receptors in the primate cerebral cortex: Possible site of action of hallucinogenic and antipsychotic drugs in pyramidal cell apical dendrites. Proc. Natl. Acad. Sci. USA *95*, 735–740.

Johnson, F.N., Ary, I.E., Teiger, D.G., and Kassel, R.J. (1973). Emetic activity of reduced lysergamides. J. Med. Chem. *16*, 532–537.

Jordan, M., Schallhorn, A., and Wurm, F.M. (1996). Transfecting mammalian cells: Optimization of critical parameters affecting calcium-phosphate precipitate formation. Nucleic Acids Res. *24*, 596–601.

Kang, Y., Zhou, X.E., Gao, X., He, Y., Liu, W., Ishchenko, A., Barty, A., White, T.A., Yefanov, O., Han, G.W., et al. (2015). Crystal structure of rhodopsin bound to arrestin by femtosecond X-ray laser. Nature *523*, 561–567.

Kenakin, T., Watson, C., Muniz-Medina, V., Christopoulos, A., and Novick, S. (2012). A simple method for quantifying functional selectivity and agonist bias. ACS Chem. Neurosci. *3*, 193–203.

Klauda, J.B., Venable, R.M., Freites, J.A., O'Connor, J.W., Tobias, D.J., Mondragon-Ramirez, C., Vorobyov, I., MacKerell, A.D., Jr., and Pastor, R.W. (2010). Update of the CHARMM all-atom additive force field for lipids: Validation on six lipid types. J. Phys. Chem. B *114*, 7830–7843.

Kroeze, W.K., Sassano, M.F., Huang, X.P., Lansu, K., McCorvy, J.D., Giguère, P.M., Sciaky, N., and Roth, B.L. (2015). PRESTO-Tango as an open-source resource for interrogation of the druggable human GPCRome. Nat. Struct. Mol. Biol. *22*, 362–369.

Li, J., Zhu, T., Cramer, C.J., and Truhlar, D.G. (1998). New Class IV Charge Model for Extracting Accurate Partial Charges from Wave Functions. J. Phys. Chem. A *102*, 1820–1831.

Liu, W., Wacker, D., Gati, C., Han, G.W., James, D., Wang, D., Nelson, G., Weierstall, U., Katritch, V., Barty, A., et al. (2013). Serial femtosecond crystallography of G protein-coupled receptors. Science *342*, 1521–1524.

Lomize, M.A., Lomize, A.L., Pogozheva, I.D., and Mosberg, H.I. (2006). OPM: Orientations of proteins in membranes database. Bioinformatics *22*, 623–625.

MacKerell, A.D., Bashford, D., Bellott, M., Dunbrack, R.L., Evanseck, J.D., Field, M.J., Fischer, S., Gao, J., Guo, H., Ha, S., et al. (1998). All-atom empirical potential for molecular modeling and dynamics studies of proteins. J. Phys. Chem. B *102*, 3586–3616.

Manglik, A., Lin, H., Aryal, D.K., McCorvy, J.D., Dengler, D., Corder, G., Levit, A., Kling, R.C., Bernat, V., Hübner, H., et al. (2016). Structure-based discovery of opioid analgesics with reduced side effects. Nature *537*, 185–190.

Masri, B., Salahpour, A., Didriksen, M., Ghisi, V., Beaulieu, J.M., Gainetdinov, R.R., and Caron, M.G. (2008). Antagonism of dopamine D2 receptor/beta-arrestin 2 interaction is a common property of clinically effective antipsychotics. Proc. Natl. Acad. Sci. USA *105*, 13656–13661.

McCoy, A.J., Grosse-Kunstleve, R.W., Adams, P.D., Winn, M.D., Storoni, L.C., and Read, R.J. (2007). Phaser crystallographic software. J. Appl. Cryst. *40*, 658–674.

Minor, W., Cymborowski, M., Otwinowski, Z., and Chruszcz, M. (2006). HKL-3000: The integration of data reduction and structure solution–from diffraction images to an initial model in minutes. Acta Crystallogr. D Biol. Crystallogr. *62*, 859–866.

Motulsky, H.J., and Mahan, L.C. (1984). The kinetics of competitive radioligand binding predicted by the law of mass action. Mol. Pharmacol. *25*, 1–9.

Murshudov, G.N., Vagin, A.A., and Dodson, E.J. (1997). Refinement of macromolecular structures by the maximum-likelihood method. Acta Crystallogr D Biol Crystallogr. *53*, 240–255.

Mysinger, M.M., and Shoichet, B.K. (2010). Rapid context-dependent ligand desolvation in molecular docking. J. Chem. Inf. Model. *50*, 1561–1573.

Mysinger, M.M., Carchia, M., Irwin, J.J., and Shoichet, B.K. (2012). Directory of useful decoys, enhanced (DUD-E): Better ligands and decoys for better benchmarking. J. Med. Chem. *55*, 6582–6594.

Nichols, D.E. (2016). Psychedelics. Pharmacol. Rev. *68*, 264–355.

Nichols, D.E., Monte, A., Huang, X., and Marona-Lewicka, D. (1996). Stereoselective pharmacological effects of lysergic acid amides possessing chirality in the amide substituent. Behav. Brain Res. *73*, 117–119.

Nichols, D.E., Frescas, S., Marona-Lewicka, D., and Kurrasch-Orbaugh, D.M. (2002). Lysergamides of isomeric 2,4-dimethylazetidines map the binding orientation of the diethylamide moiety in the potent hallucinogenic agent N,N-diethyllysergamide (LSD). J. Med. Chem. *45*, 4344–4349.

Otwinowski, Z., and Minor, W. (1997). Processing of X-ray diffraction data collected in oscillation mode. Methods Enzymol. *276*, 307–326.

Passie, T., Halpern, J.H., Stichtenoth, D.O., Emrich, H.M., and Hintzen, A. (2008). The pharmacology of lysergic acid diethylamide: A review. CNS Neurosci. Ther. *14*, 295–314.

Pei, J., and Grishin, N.V. (2014). PROMALS3D: Multiple protein sequence alignment enhanced with evolutionary and three-dimensional structural information. Methods Mol. Biol. *1079*, 263–271.

Perez-Aguilar, J.M., Shan, J., LeVine, M.V., Khelashvili, G., and Weinstein, H. (2014). A functional selectivity mechanism at the serotonin-2A GPCR involves ligand-dependent conformations of intracellular loop 2. J. Am. Chem. Soc. *136*, 16044–16054.

Ranganathan, A., Dror, R.O., and Carlsson, J. (2014). Insights into the role of Asp79(2.50) in β2 adrenergic receptor activation from molecular dynamics simulations. Biochemistry *53*, 7283–7296.

Rasmussen, S.G., Choi, H.J., Fung, J.J., Pardon, E., Casarosa, P., Chae, P.S., Devree, B.T., Rosenbaum, D.M., Thian, F.S., Kobilka, T.S., et al. (2011a). Structure of a nanobody-stabilized active state of the β(2) adrenoceptor. Nature *469*, 175–180.

Rasmussen, S.G., DeVree, B.T., Zou, Y., Kruse, A.C., Chung, K.Y., Kobilka, T.S., Thian, F.S., Chae, P.S., Pardon, E., Calinski, D., et al. (2011b). Crystal structure of the β2 adrenergic receptor-Gs protein complex. Nature *477*, 549–555.

Roe, D.R., and Cheatham, T.E., 3rd. (2013). PTRAJ and CPPTRAJ: Software for processing and analysis of molecular dynamics trajectory data. J. Chem. Theory Comput. *9*, 3084–3095.

Rosenbaum, D.M., Zhang, C., Lyons, J.A., Holl, R., Aragao, D., Arlow, D.H., Rasmussen, S.G., Choi, H.J., Devree, B.T., Sunahara, R.K., et al. (2011). Structure and function of an irreversible agonist-β(2) adrenoceptor complex. Nature *469*, 236–240.

Roth, B.L., Baner, K., Westkaemper, R., Siebert, D., Rice, K.C., Steinberg, S., Ernsberger, P., and Rothman, R.B. (2002). Salvinorin A: A potent naturally occurring nonnitrogenous kappa opioid selective agonist. Proc. Natl. Acad. Sci. USA *99*, 11934–11939.

Roth, C.B., Hanson, M.A., and Stevens, R.C. (2008). Stabilization of the human beta2-adrenergic receptor TM4-TM3-TM5 helix interface by mutagenesis of Glu122(3.41), a critical residue in GPCR structure. J. Mol. Biol. *376*, 1305–1319.

Sadowski, J., Gasteiger, J., and Klebe, G. (1994). Comparison of automatic three-dimensional model builders using 639 X-ray structures. J. Chem. Inf. Comput. Sci. *34*, 1000–1008.

Schmid, Y., Enzler, F., Gasser, P., Grouzmann, E., Preller, K.H., Vollenweider, F.X., Brenneisen, R., Müller, F., Borgwardt, S., and Liechti, M.E. (2015). Acute effects of lysergic acid diethylamide in healthy subjects. Biol. Psychiatry *78*, 544–553.

Sewell, R.A., Halpern, J.H., and Pope, H.G., Jr. (2006). Response of cluster headache to psilocybin and LSD. Neurology *66*, 1920–1922.

Sharp, K.A. (1995). Polyelectrolyte electrostatics: Salt dependence, entropic, and enthalpic contributions to free energy in the nonlinear Poisson–Boltzmann model. Biopolymers *36*, 227–243.

Shaw, E., and Woolley, D.W. (1956). Some serotoninlike activities of lysergic acid diethylamide. Science *124*, 121–122.

Shimamura, T., Shiroishi, M., Weyand, S., Tsujimoto, H., Winter, G., Katritch, V., Abagyan, R., Cherezov, V., Liu, W., Han, G.W., et al. (2011). Structure of the human histamine H1 receptor complex with doxepin. Nature *475*, 65–70.

Southan, C., Sharman, J.L., Benson, H.E., Faccenda, E., Pawson, A.J., Alexander, S.P., Buneman, O.P., Davenport, A.P., McGrath, J.C., Peters, J.A., et al.; NC-IUPHAR (2016). The IUPHAR/BPS Guide to PHARMACOLOGY in 2016: Towards curated quantitative interactions between 1300 protein targets and 6000 ligands. Nucleic Acids Res. *44*(D1), D1054–D1068.

Stoll, A., and Hofmann, A. (1955). Amide Der Stereoisomeren Lysergsauren Und Dihydro-Lysergsauren 0.38. Mitteilung Uber Mutterkornalkaloide. Helv. Chim. Acta *38*, 421–433.

Titeler, M., Lyon, R.A., and Glennon, R.A. (1988). Radioligand binding evidence implicates the brain 5-HT2 receptor as a site of action for LSD and phenylisopropylamine hallucinogens. Psychopharmacology (Berl.) *94*, 213–216.

Urban, J.D., Clarke, W.P., von Zastrow, M., Nichols, D.E., Kobilka, B., Weinstein, H., Javitch, J.A., Roth, B.L., Christopoulos, A., Sexton, P.M., et al. (2007). Functional selectivity and classical concepts of quantitative pharmacology. J. Pharmacol. Exp. Ther. *320*, 1–13.

Vane, J.R. (1957). A sensitive method for the assay of 5-hydroxytryptamine. Br. Pharmacol. Chemother. *12*, 344–349.

Vanommeslaeghe, K., and MacKerell, A.D., Jr. (2012). Automation of the CHARMM General Force Field (CGenFF) I: Bond perception and atom typing. J. Chem. Inf. Model. *52*, 3144–3154.

Vanommeslaeghe, K., Hatcher, E., Acharya, C., Kundu, S., Zhong, S., Shim, J., Darian, E., Guvench, O., Lopes, P., Vorobyov, I., and Mackerell, A.D., Jr. (2010). CHARMM general force field: A force field for drug-like molecules compatible with the CHARMM all-atom additive biological force fields. J. Comput. Chem. *31*, 671–690.

Vanommeslaeghe, K., Raman, E.P., and MacKerell, A.D., Jr. (2012). Automation of the CHARMM General Force Field (CGenFF) II: Assignment of bonded parameters and partial atomic charges. J. Chem. Inf. Model. *52*, 3155–3168.

Verhoeff, N.P., Visser, W.H., Ferrari, M.D., Saxena, P.R., and van Royen, E.A. (1993). Dopamine D2-receptor imaging with 123I-iodobenzamide SPECT in migraine patients abusing ergotamine: Does ergotamine cross the blood brain barrier? Cephalalgia *13*, 325–329.

Violin, J.D., and Lefkowitz, R.J. (2007). Beta-arrestin-biased ligands at seven-transmembrane receptors. Trends Pharmacol. Sci. *28*, 416–422.

Wacker, D., Fenalti, G., Brown, M.A., Katritch, V., Abagyan, R., Cherezov, V., and Stevens, R.C. (2010). Conserved binding mode of human beta2 adrenergic receptor inverse agonists and antagonist revealed by X-ray crystallography. J. Am. Chem. Soc. *132*, 11443–11445.

Wacker, D., Wang, C., Katritch, V., Han, G.W., Huang, X.P., Vardy, E., McCorvy, J.D., Jiang, Y., Chu, M., Siu, F.Y., et al. (2013). Structural features for functional selectivity at serotonin receptors. Science *340*, 615–619.

Wang, C., Jiang, Y., Ma, J., Wu, H., Wacker, D., Katritch, V., Han, G.W., Liu, W., Huang, X.P., Vardy, E., et al. (2013). Structural basis for molecular recognition at serotonin receptors. Science *340*, 610–614.

Webb, B., and Sali, A. (2014). Comparative Protein Structure Modeling Using MODELLER. Current protocols in bioinformatics / editoral board, Andreas D Baxevanis [et al] *47*, 5 6 1-5 6 32.

Woolley, D.W., and Shaw, E. (1954). A biochemical and pharmacological suggestion about certain mental disorders. Proc. Natl. Acad. Sci. USA *40*, 228–231.

Wootten, D., Reynolds, C.A., Smith, K.J., Mobarec, J.C., Koole, C., Savage, E.E., Pabreja, K., Simms, J., Sridhar, R., Furness, S.G., et al. (2016). The extracellular surface of the GLP-1 receptor is a molecular trigger for biased agonism. Cell *165*, 1632–1643.

Word, J.M., Lovell, S.C., Richardson, J.S., and Richardson, D.C. (1999). Asparagine and glutamine: Using hydrogen atom contacts in the choice of side-chain amide orientation. J. Mol. Biol. *285*, 1735–1747.

Zhang, L., and Hermans, J. (1996). Hydrophilicity of cavities in proteins. Proteins *24*, 433–438.

STAR★METHODS

KEY RESOURCES TABLE

REAGENT or RESOURCE	SOURCE	IDENTIFIER
Antibodies		
gp64-PE antibody	Expression Systems	Cat#97-201
Chemicals, Peptides, and Recombinant Proteins		
AEBSF	GoldBio	A-540-5
Leupeptin	Sigma	L2884
E-64	AG Scientific	E-2030
Aprotinin	GoldBio	A-655-100
Iodoacetamide	Sigma	Cat#I1149
n-dodecyl-beta-D-maltopyranoside (DDM)	Anatrace	Cat#D310
Cholesterol hemisucinate (CHS)	Sigma	Cat#C6512
TALON IMAC resin	Clontech	Cat#635507
1-Oleoyl-rac-glycerol (monoolein)	Sigma	Cat#M7765
Cholesterol	Sigma	Cat#C8667
Fluo-4 Direct dye	Invitrogen	Cat#F10473
BrightGlo	Promega	Cat#E2620
RNA binding yttrium silicate beads	PerkinElmer	Cat#RPNQ0013
Coelenterazine 400a (Deep Blue C)	Nanolight	Cat#340-1
[^{3}H]-LSD	Perkin Elmer	Cat#NET638
[^{3}H]-myo-inositol	Perkin Elmer	Cat#NET114A005
SB 206553	Tocris	Cat#1661
Poly-L-lysine	Sigma	Cat#P2636
Tetracycline	Sigma	Cat#T7660
Polyethyleneimine (PEI) solution	Sigma	Cat#P3143
Penicillin/Streptomycin	Invitrogen	Cat#15140-122
Hygromycin B	KSE Scientific	Cat#98-923
Blasticydin	Invivogen	Cat#ant-bl-10p
Zeocin	Invitrogen	Cat#R25005
Sf-900 II SFM	Invitrogen	Cat#10902096
ESF921	Expression Systems	Cat#96-001-01
inositol-free DMEM	Caisson Labs	Cat#DML13
DMEM	VWR	Cat#45000-306
FBS	VWR	Cat#97068-085
Dialyzed FBS	Omega Scientific	Cat#FB-03
10xHBSS	Invitrogen	Cat#14065-056
Cellfectin II Reagent	Invitrogen	Cat#10362-100
His-tagged PreScission protease	GenScript	Cat#Z03092-500
Critical Commercial Assays		
Bac-to-Bac Baculovirus Expression system	Invitrogen	Cat#A11100
QuikChange site-directed mutagenesis	Agilent Technologies	Cat#200519
Deposited Data		
5-HT$_{2B}$R/LSD complex structure	This paper	PDB: 5TVN
Experimental Models: Cell Lines		
HEK293T	ATCC	Cat#CRL-3216
Sf9 cells	Expression Systems	Cat#94-001S

(*Continued on next page*)

Continued

REAGENT or RESOURCE	SOURCE	IDENTIFIER
HTLA	Dr. Richard Axel, Columbia Univ	N/A
Flp-In T-Rex 293 Cell Line	Invitrogen	Cat#R78007
Software and Algorithms		
AMBER	(Case et al., 2015)	http://ambermd.org/
AMSOL	(Li et al., 1998)	https://comp.chem.umn.edu/amsol/
CGenFF	(Vanommeslaeghe and MacKerell, 2012; Vanommeslaeghe et al., 2012)	https://cgenff.paramchem.org/
COOT	(Emsley et al., 2010)	www2.mrc-lmb.cam.ac.uk/personal/pemsley/coot
Corina	Molecular Networks GmbH (Sadowski et al., 1994)	https://www.mn-am.com/products/corina
CPPTRAJ	(Roe and Cheatham, 2013)	http://ambermd.org/
DOCK3.7	(Coleman et al., 2013)	http://dock.compbio.ucsf.edu
Dowser	(Zhang and Hermans, 1996)	http://danger.med.unc.edu/hermans/dowser/dowser.htm
DUD-E	(Mysinger et al., 2012)	http://dude.docking.org/
HKL2000	(Otwinowski and Minor, 1997)	http://www.hkl-xray.com/
IUPHAR	(Southan et al., 2016)	http://www.guidetopharmacology.org/
Marvin v.15.11.23.0	ChemAxon	https://www.chemaxon.com
MODELER-9v15	(Webb and Sali, 2014)	https://salilab.org/modeller/
Omega	OpenEye Scientific Software (Hawkins et al., 2010)	http://www.eyesopen.com/omega
Phaser	(McCoy et al., 2007)	http://www.ccp4.ac.uk
Phenix	(Adams et al., 2010)	https://www.phenix-online.org
Prime	Schrödinger	https://www.schrodinger.com/
Prism v.5.0	GraphPad Software Inc.	N/A
PROMALS3D	(Pei and Grishin, 2014)	http://prodata.swmed.edu/promals3d/promals3d.php
QNIFFT	(Gallagher and Sharp, 1998)	http://crystal.med.upenn.edu/software.html
Reduce	(Word et al., 1999)	http://kinemage.biochem.duke.edu/software/reduce.php
REFMAC	(Murshudov et al., 1997)	http://www.ccp4.ac.uk
VMD	(Humphrey et al., 1996)	http://www.ks.uiuc.edu/Research/vmd/
Other		
100 kDa molecular weight cut-off Vivaspin 20 concentrator	Sartorius Stedim	Cat#VS2042
PD MiniTrap G-25 columns	GE Healthcare	Cat#28-9180-07
100 kDa molecular weight cut-off Vivaspin 500 centrifuge concentrator	Sartorius Stedim	Cat#VS0142
96-well LCP glass sandwich set	Marienfeld GmbH	Cat#0890003
384-well black plates	Greiner Bio-one GmbH	Cat#781091
384-well white plates	Greiner Bio-one GmbH	Cat#781098
96-well black plates	Greiner Bio-one GmbH	Cat#655090
Meltilex	Perkin Elmer	Cat#1450-441
Filtermat A	Perkin Elmer	Cat#1450-421

CONTACT FOR REAGENT AND RESOURCE SHARING

Further information and requests for reagents should be directed to and will be fulfilled by the Lead Contact, Bryan L. Roth (bryan_roth@med.unc.edu).

METHOD DETAILS

Generation of 5-HT_{2B}R receptor crystallization construct

Crystallization of the 5-HT_{2B}R/LSD complex was done based on a previously engineered receptor construct that was edited by Quickchange PCR. Using site-directed mutagenesis we added the ICL3 residue V313 to a previously published construct (Liu et al., 2013) that had been synthesized by DNA2.0. The final construct a) lacks N-terminal residues 1-35, b) lacks C-terminal residues 406-481, c) contains a thermostabilizing $M144W^{3.41}$ mutation (Roth et al., 2008), and d) contains A1-L106 of the thermostabilized apocytochrome b_{562} RIL (BRIL) from *E. coli* (M7W, H102I, R106L) in place of receptor residues Y249-S312 of ICL3 (Chun et al., 2012). Further modifications are a haemagglutinin (HA) signal sequence followed by a FLAG tag at the N terminus, and a PreScission protease site followed by a 10 × His tag at the C terminus to enable purification by immobilized metal affinity chromatography.

Expression and purification of 5-HT_{2B}R

High-titer recombinant baculovirus (> 10^9 viral particles per ml) was generated using the Bac-to-Bac Baculovirus Expression System (Invitrogen). Recombinant baculovirus was obtained by transfecting ~5 μg of recombinant bacmid into 5x10^5 settled *Spodoptera frugiperda* (Sf9) cells (Expression Systems) in a 24 well plate (Corning) using 3 μl Cellfectin II Reagent (Invitrogen). After 5-12 hr, media was exchanged for 1 mL Sf-900 II SFM media (Invitrogen) and incubated for 4-6 days at 27°C. P0 viral stock with ~10^9 virus particles per ml was harvested as the supernatant and used to generate high-titer baculovirus stock by infection of 40-1000 mls of Sf9 cells and incubation for several days. Viral titers were determined by flow-cytometric analysis of cells stained with gp64-PE antibody (Expression Systems) (Hanson et al., 2007). Expression of 5-HT_{2B}R was carried out by infection of Sf9 cells at a cell density of 2-3 × 10^6 cells/ml in ESF921 media (Expression Systems) with P1 or P2 virus at a MOI (multiplicity of infection) of 3-5. Cells were harvested by centrifugation at 48 hr post infection, washed in PBS, and stored at −80°C until use. Cells were disrupted by thawing frozen cell pellets in a hypotonic buffer containing 10 mM HEPES, pH 7.5, 10 mM $MgCl_2$, 20 mM KCl and protease inhibitors (500 μM AEBSF, 1 μM E-64, 1 μM Leupeptin, 150 nM Aprotinin). Membranes were purified by repeated centrifugation in a high osmolarity buffer containing 1.0 M NaCl, 10 mM HEPES, pH 7.5, 10 mM $MgCl_2$, 20 mM KCl, to remove soluble and membrane associated proteins. Purified membranes were directly flash-frozen in liquid nitrogen and stored at −80°C.

Purified membranes were resuspended in buffer containing 10 mM HEPES, pH 7.5, 10 mM $MgCl_2$, 20 mM KCl, 150 mM NaCl, 50 μM LSD (synthesized in house), and protease inhibitors, and incubated at room temperature for 1 hr. After 30 min incubation in the presence of 2 mg/ml iodoacetamide (Sigma), membranes were solubilized in 10 mM HEPES, pH 7.5, 150 mM NaCl, 1% (w/v) n-dodecyl-β-D-maltopyranoside (DDM, Anatrace), 0.2% (w/v) cholesteryl hemisuccinate (CHS, Sigma), 25 μM LSD, and protease inhibitors for 2 hr at 4°C. Unsolubilized material was removed by centrifugation at 150,000 × g for 30 min, and 15 mM imidazole was added to the supernatant. Proteins were bound to TALON IMAC resin (Clontech) overnight at 4°C using approximately 750 μl resin for protein purified from 1 L of cells. The resin was then washed with 10 column volumes (cv) of Wash Buffer I (50 mM HEPES, pH 7.5, 800 mM NaCl, 0.1% (w/v) DDM, 0.02% (w/v) CHS, 20 mM imidazole, 10% (v/v) glycerol, and 20 μM LSD, followed by 10 cv of Wash Buffer II (25 mM HEPES, pH 7.5, 500 mM NaCl, 0.05% (w/v) DDM, 0.01% (w/v) CHS, 10% (v/v) glycerol, and 20 μM LSD). Proteins were eluted in 2.5 cv of Wash Buffer II + 250 mM imidazole, concentrated in a 100 kDa molecular weight cut-off Vivaspin 20 concentrator (Sartorius Stedim) to 500 μl, and imidazole was removed by desalting the protein over PD MiniTrap G-25 columns (GE Healthcare). The C-terminal 10 × His-tag was removed by addition of His-tagged PreScission protease (GenScript) and incubation overnight at 4°C. Protease, cleaved His-tag and uncleaved protein were removed by passing the suspension through equilibrated TALON IMAC resin (Clontech) and collecting the flow-through. 5-HT_{2B}R/LSD complexes were then concentrated to ~40 mg/ml with a 100 kDa molecular weight cut-off Vivaspin 500 centrifuge concentrator (Sartorius Stedim). Protein purity and monodispersity were tested by analytical size-exclusion chromatography.

Lipidic cubic phase crystallization

Purified and concentrated 5-HT_{2B}R/LSD complexes were reconstituted into lipidic cubic phase (LCP) by mixing detergent solubilized protein with a molten monoolein/cholesterol mixture (90%/10%) in a volume ratio of 2:3 using the twin-syringe method (Caffrey and Cherezov, 2009): two 100 ul gas-tight pipettes (Hamilton) carrying protein and molten lipids were connected through a thin capillary (made in-house), and contents of one pipette were dispensed into the other and the protein/lipid mix was then repeatedly squeezed through the capillary until a transparent homogeneous paste was obtained. Crystallization was done on 96-well glass sandwich plates (Marienfeld GmbH) in 50 nL LCP drops dispensed from a 10 ul gas-tight pipette (Hamilton) using a handheld dispenser (Art Robbins Instruments) and overlaid with 1 μl of precipitant solution. Upon optimization, 5-HT_{2B}R/LSD crystals were obtained in 100 mM Tris/HCl pH 7.5-8.0, 90-130 mM potassium phosphate monobasic, 28%–30% PEG400. Crystals grew to a maximum size of 70 μm × 30 μm × 20 μm within three days and were harvested directly from the LCP matrix using MiTeGen micromounts before flash-freezing and storage in liquid nitrogen.

Data collection, structure solution, and refinement

X-ray data were collected at the 23ID-B and 23ID-D beamline (GM/CA CAT) at the Advanced Photon Source, Argonne, IL using a 10 μm minibeam at a wavelength of 1.0330 Å and a MarMosaic 300 CCD detector. Diffraction data were collected by exposing the crystals for 1-3 s to unattenuated beam using 1° oscillation. A full dataset was assembled from nine crystals due to rapid onset

of radiation decay at such high doses. Data were indexed, integrated, scaled, and merged using HKL3000 (Minor et al., 2006), and initial phases were obtained by molecular replacement in PHASER (McCoy et al., 2007) using two independent search models - a truncated model of the 7TM portion of the 5-HT_{2B}R/ERG complex (PDB ID: 4IB4), and the thermostabilized apocytochrome b_{562}RIL protein (PDB ID: 1M6T) (Chu et al., 2002). Refinement was performed with PHENIX (Adams et al., 2010) and REFMAC followed by manual examination and rebuilding of the refined coordinates in the program COOT (Emsley et al., 2010) using $|2F_o|$ - $|F_c|$, $|F_o|$ - $|F_c|$, and omit maps.

LSD synthesis

LSD was synthesized by the method of Johnson et al. (Johnson et al., 1973) as follows. All operations were carried out under conditions of reduced light. A slurry of 315 mg (1.0 mmol) d-lysergic acid monohydrate (Farmitalia) in 20 mL of anhyd. $CHCl_3$ in a 50 mL 3-necked flask fitted with a reflux condenser was stirred under N_2 and heated to reflux on a 90°C oil bath. Diethylamine 731 mg (10 mmol) in 2.5 mL of $CHCl_3$ and 307 mg (2 mmol) of $POCl_3$ in 2.5 mL of $CHCl_3$, were added simultaneously from separate dropping funnels over about 2 min. The reaction was kept at reflux for another 5 min until a clear, dark amber solution resulted. After cooling to RT the solution was washed with 20 mL of 1 N NH_4OH. The chloroform solution was dried overnight over Na_2SO_4. TLC (7:3 CHCl2-Me2CO; alumina plate) of the dried solution showed a fast-moving bright blue fluorescent product spot, and a smaller light blue fluorescent spot at lower Rf (iso-LSD). The solution was filtered to remove drying agent and concentrated under reduced pressure to afford a brown viscous residue. The crude product thus obtained was purified by centrifugal thin layer chromatography (Chromatotron, Harrison Research), using a 2 mm silica plate, under a N_2/NH_3 atmosphere (N_2 bubbled through concentrated NH_4OH), and eluting with 100% CH_2Cl_2 (Nichols et al., 2002). The bright blue fluorescent band that eluted first was collected and concentrated by rotary vacuum evaporation and pumped under high vacuum overnight. It was a single blue fluorescent spot on TLC (7:3 CH_2Cl_2-Me_2CO; alumina plate). The crude base was dissolved in a minimum volume of reagent MeOH and 0.5 equivalent of L-(+)-tartaric acid was added. The solution was swirled at room temp until complete solution, was diluted with six volumes of anhyd. ethyl acetate, and placed into the cold room overnight whereupon the tartrate salt crystallized as fine needles. The crystals were collected by suction filtration, washed on the filter with EtOAc, and air-dried to afford 283.2 mg (71%) of crystalline product as the solvate with 2 molecules of MeOH. After drying under high vacuum, the LSD tartrate had a mp of 197-199°C and a Lit mp (Stoll and Hofmann, 1955) of 198-200°C.

Calcium flux assay

Stable cell lines for 5-HT_{2B}R and 5-HT_{2A}R constructs were generated using the Flp-In 293 T-Rex Tetracycline inducible system (Invitrogen). Receptor mutants were generated as previously described (Wang et al., 2013). Tetracycline-induced cells were seeded in 384-well poly-L-lysine plates at a density of 10,000 cells/well in DMEM containing 1% dialyzed FBS at least 16-24 hr before the calcium flux assay. On the day of the assay, the cells were incubated (20 μl/well) for 1 hr at 37°C with Fluo-4 Direct dye (Invitrogen) reconstituted in FLIPR buffer (1 × HBSS, 2.5 mM probenecid, and 20 mM HEPES, pH 7.4). After dye loading, cells were placed in a $FLIPR^{TETRA}$ fluorescence imaging plate reader (Molecular Dynamics). Drug dilutions were prepared at 3 × final concentration in drug buffer (1 × HBSS, 20 mM HEPES, 0.1% BSA, 0.01% ascorbic acid, pH 7.4) and aliquoted into 384-well plates and placed in the $FLIPR^{TETRA}$ for drug stimulation. Drug solutions used for FLIPR assay were exactly the same as used for the Tango assay. The fluidics module and plate reader of the $FLIPR^{TETRA}$ were programmed to read baseline fluorescence for 10 s (1 read/s), then 10 μl of drug/well was added and read for 5 min (1 read/s). Fluorescence in each well was normalized to the average of the first 10 reads (i.e., baseline fluorescence). Then, the maximum-fold increase, which occurred within the first 60 s after drug addition, was determined and fold over baseline was plotted as a function of drug concentration. Data were normalized to % 5-HT stimulation and analyzed using ''log(agonist) vs. response'' in Graphpad Prism 5.0.

Tango arrestin recruitment assay

The 5-HT_{2B}R and 5-HT_{2A}R Tango constructs, which contain the TEV cleavage site and the tetracycline transactivator (tTA) fused to the C terminus of the receptor, were designed and assays were performed as previously described (Kroeze et al., 2015; Wacker et al., 2013). HTLA cells expressing TEV fused-β-Arrestin2 and a tetracycline transactivator-driven luciferase (kindly provided by Dr. Richard Axel, Columbia Univ.) were grown in HTLA media (10% FBS DMEM containing 5 μg/mL Puromycin and 100 μg/mL Hygromycin B). The day before transfection, HTLA cells were split to yield approximately $9x10^6$ cells/15-cm plate next day. On the day of transfection, media from 15-cm plates was removed, cells were washed with 10 mL of PBS, and media was replaced with DMEM containing 10% dialyzed FBS. After one hour, cells were transfected with 15 μg per 15-cm of either 5-HT_{2B}R or 5-HT_{2A}R Tango construct using the calcium phosphate transfection method (Jordan et al., 1996). The next day, media and transfection reagents were removed, cells were washed with PBS, dissociated using trypsin, centrifuged and resuspended in DMEM supplemented with 1% dialyzed FBS. Transfected cells were then plated onto poly-L-lysine-coated 384-well white clear bottom cell culture plates at a density of 10,000 cells/well in a total of 40 μl. The cells were incubated for at least 6 hr before receiving drug stimulation to allow for recovery and adherence to the plate. Drug solutions were prepared in drug buffer (1 × HBSS, 20 mM HEPES, 0.1% BSA, 0.01% ascorbic acid, pH 7.4) at 3 × and added to cells (20 μl per well) for overnight incubation. Drug solutions used for the Tango assay were exactly the same as used for the FLIPR assay, which was conducted in parallel to the Tango assay. After 20-22 hr overnight incubation, media and drug solutions were removed from plates and 20 μl per well of BrightGlo reagent (purchased from Promega, after

1:20 dilution) was added per well. The plate was incubated for 20 min at room temperature in the dark before being counted using a luminescence counter. Results (relative luminescence units) were plotted as a function of drug concentration, normalized to % 5-HT stimulation, and analyzed using ''log(agonist) vs. response'' in GraphPad Prism 5.0.

Phosphoinositide hydrolysis assay

Phosphoinositide (PI) hydrolysis assays measuring inositol phosphates (IP) were performed using the scintillation proximity assay (Bourdon et al., 2006; Huang et al., 2009). On the day before the assay, cells were seeded into 96-well poly-lysine coated plates at a density of 40-50,000 cells/well in 100 μL inositol-free DMEM containing 1% dialyzed FBS. After 6 hr, an additional 100 μL of label media was added containing 1 μCi/well (final concentration) of [^{3}H]-myo-inositol (PerkinElmer) in inositol-free DMEM (Caisson Labs) containing 1% dialyzed FBS and plates were incubated overnight for 16-18 hr at 37°C and 5% CO_2. The next day, label media was removed and cells were washed twice with 60 uL of drug buffer (1 × HBSS, 20 mM HEPES, 0.1% BSA, 0.01% ascorbic acid, pH 7.4), then 60 uL of drug buffer was added per well. Afterward, 30 uL of drug (3X) was added per well and incubated at 37°C for various time durations at 37°C. To capture IP accumulation, lithium chloride (10 μL/well, 15 mM final concentration) was added 15 min before lysis. The assay was terminated by replacement of the incubation medium with 40 μL of 50 mM formic acid. After overnight incubation at 4°C, 10 μL of lysates were added to 96-well flexible, clear microplates (PerkinEmer) containing 75 μL of 0.2 mg/well RNA binding yttrium silicate beads (PerkinElmer), and incubated for 1 hr on a shaker. Afterward, plates were centrifuged at 300xg for 1 min, and radioactivity was measured using a Wallac MicroBeta Trilux plate reader (PerkinElmer). Data were plotted as counts per minute (CPM) as a function of drug concentration, normalized to % 5-HT stimulation, and analyzed using ''log(agonist) vs. response'' in GraphPad Prism 5.0.

Bioluminescence resonance energy transfer arrestin assay

To measure 5-HT_{2B}R-mediated β-arrestin2 recruitment, HEK293T cells were co-transfected in a 1:1:15 ratio with human 5-HT_{2B}R containing C-terminal *Renilla* luciferase (*R*Luc8), GRK2, and Venus-tagged N-terminal β-arrestin2. After at least 24 hr, transfected cells were plated in poly-lysine coated 96-well white clear bottom cell culture plates in plating media (DMEM + 1% dialyzed FBS) at a density of 40-50,000 cells in 200 μl per well and incubated overnight. The next day, media was decanted and cells were washed twice with 60 μL of drug buffer (1 × HBSS, 20 mM HEPES, 0.1% BSA, 0.01% ascorbic acid, pH 7.4), then 60 μL of drug buffer was added per well. For kinetic experiments, plates were incubated at 37°C at least 20 min prior to receiving drug stimulation. Afterward, 30 μL of drug (3X) was added per well and incubated for designated time points. Before reading, 10 μL of the *R*Luc substrate, coelenterazine h (Promega, 5 μM final concentration) was added per well, incubated an additional 5 min to allow for substrate diffusion, and plates were immediately read for both luminescence at 485 nm and fluorescent eYFP emission at 530 nm for 1 s per well using a Mithras LB940 multimode microplate reader. The ratio of eYFP/*R*Luc was calculated per well and the net BRET ratio was calculated by subtracting the eYFP/*R*Luc per well from the eYFP/*R*Luc ratio in wells without Venus-β-Arrestin present. The net BRET ratio was plotted as a function of drug concentration using Graphpad Prism 5 (Graphpad Software Inc., San Diego, CA). Data were normalized to % 5-HT stimulation and analyzed using nonlinear regression ''log(agonist) vs. response'' in GraphPad Prism 5.0.

Ligand association and dissociation radioligand binding assays

Radioligand dissociation and association assays were performed in parallel utilizing the same concentrations of radioligand, membrane preparations, and binding buffer (50 mM Tris, 10 mM $MgCl_2$, 0.1 mM EDTA, 0.1% BSA, 0.01% ascorbic acid, pH 7.4). All assays utilized at least 2-4 concentrations of radioligand ([^{3}H]-LSD = 0.2-5.0 nM) (PerkinElmer). For dissociation assays, membranes were incubated with radioligand for at least 2 hr at 37°C (unless otherwise indicated) before the addition of 10 μL of 10 μM excess cold ligand to the 200 μL membrane suspension at designated time points. For association experiments, 100 μL of radioligand was added to 100 μL membrane suspensions at designated time points. Time points spanned 2 min to 12 hr, depending on experimental conditions and radioligand. For the determination of k_{on} and k_{off} for unlabeled ergotamine (ERG), membranes of either 5-HT_{2B}R or 5-HT_{2B}R L209A^{EL2} were incubated with [^{3}H]-LSD and several concentrations of ergotamine. Non-specific binding was determined by addition of 10 μM SB 206553 for 5-HT_{2B}R, or 10 μM spiperone for 5-HT_{2A}R. Immediately at time = 0 min, plates were harvested by vacuum filtration onto 0.3% polyethyleneimine pre-soaked 96-well filter mats (Perkin Elmer) using a 96-well Filtermate harvester, followed by three washes of cold wash buffer (50 mM Tris, pH 7.4). Scintillation (Meltilex) cocktail (Perkin Elmer) was melted onto dried filters and radioactivity was counted using a Wallac Trilux MicroBeta counter (PerkinElmer). Data were analyzed using ''Dissociation – One phase exponential decay'' or ''Association kinetics – Two or more concentrations of hot radioligand'' in Graphpad Prism 5.0. The previously determined [^{3}H]-LSD k_{on} and k_{off} rates of 5-HT_{2B}R or 5-HT_{2B}R L209A^{EL2} was used to estimate the k_{on} and k_{off} rates of ergotamine using the ''Kinetics of competitive binding'' equation in Graphpad Prism 5.0 as put forth by Motulsky and Mahan (Motulsky and Mahan, 1984).

MD simulations set-up

Simulations of 5-HT_{2B}R were based on both an ERG-bound crystal structure (PDB ID: 4NC3) (Liu et al., 2013) and the LSD-bound crystal structure described in this manuscript. The receptor was simulated in five distinct conditions (Table S1): (A) the LSD-bound crystal structure described in the manuscript; (B) the same structure with the ligand removed; (C) the LSD-bound crystal structure

with the L209A^{EL2} mutation; (D) the LSD-bound crystal structure with the L209A^{EL2} mutation and the ligand removed; and (E) the ERG-bound crystal structure with the ligand removed. Coordinates were prepared by first removing the crystallized BRIL fragment and non-receptor molecules except for LSD (when applicable), the cholesterol neighboring helix VII, and crystallographic water molecules within or near the receptor. For unliganded simulation conditions, ERG or LSD was removed. Prime (Schrödinger, Inc.) was used to model in missing side-chains and the missing EL2 residues D198^{EL2}, V199^{EL2}, and D200^{EL2}. Hydrogen atoms were added, and protein chain termini were capped with the neutral groups acetyl and methylamide.

In the simulations reported in this paper, titratable residues were left in their dominant protonation state at pH 7.0. In particular, all aspartate residues were deprotonated. Previous studies have suggested that, in the β2 adrenergic receptor, residues D$^{2.50}$ and D$^{3.49}$ may be deprotonated in the inactive state and protonated in the active state (Ghanouni et al., 2000; Ranganathan et al., 2014). Because the ideal protonation state is uncertain in this case, we performed additional simulations with D100$^{2.50}$ and D152$^{3.49}$ protonated (and all other titratable residues were left in their dominant protonation state at pH 7.0). We did not observe any significant differences between simulations with D100$^{2.50}$ and D152$^{3.49}$ protonated and simulations with D100$^{2.50}$ and D152$^{3.49}$ deprotonated.

In the liganded simulations, the LSD tertiary amine nitrogen was protonated, corresponding to the dominant protonation state at pH 7.0 and enabling formation of the conserved salt bridge with neighboring D135$^{3.32}$.

The prepared protein structures were aligned on the transmembrane helices to the Orientation of Proteins in Membranes (OPM) (Lomize et al., 2006) structure of PDB 4NC3, and internal waters added with Dowser (Zhang and Hermans, 1996). The structures were then inserted into a pre-equilibrated palmitoyl-oleoyl-phosphatidylcholine (POPC) bilayer, and solvated with 0.15 M NaCl in explicitly represented water, then neutralized by removing sodium ions. Final system dimensions were approximately 80 × 70 × 120 Å^3, including about 120 lipids, 29 sodium ions, 32 chloride ions, and 12,000 water molecules.

MD simulation force field parameters

We used the CHARMM36 parameter set for protein molecules, lipid molecules, and salt ions, and the CHARMM TIP3P model for water; protein parameters incorporated CMAP terms (Best et al., 2012a; Best et al., 2012b; Huang and MacKerell, 2013; Klauda et al., 2010; MacKerell et al., 1998). Parameters for LSD were generated using the CHARMM General Force Field (CGenFF) (Vanommeslaeghe et al., 2010, 2012; Vanommeslaeghe and MacKerell, 2012) with the ParamChem server (paramchem.org), version 1.0.0. Full parameter sets are available upon request.

MD simulation protocol

Simulations were performed on GPUs using the CUDA version of PMEMD (Particle Mesh Ewald Molecular Dynamics) in Amber15 (Case et al., 2015). Prepared systems were minimized, then equilibrated as follows: The system was heated using the Langevin thermostat from 0 to 100K in the NVT ensemble over 12.5 ps with harmonic restraints of 10.0 kcal·mol^{-1}·Å^{-2} on the non-hydrogen atoms of lipid, protein, and ligand, and initial velocities sampled from the Boltzmann distribution. The system was then heated to 310K over 125 ps in the NPT ensemble with semi-isotropic pressure coupling and a pressure of one bar. Further equilibration was performed at 310 K with harmonic restraints on the protein and ligand starting at 5.0 kcal·mol^{-1}·Å^{-2} and reduced by 1.0 kcal·mol^{-1}·Å^{-2} in a stepwise fashion every 2 ns, for a total of 10 ns of additional restrained equilibration.

Multiple simulations were initialized from the final snapshot of the restrained equilibration for each of the five conditions, for a total of 36 simulations (Table S1). These simulations were conducted in the NPT ensemble at 310 K and 1 bar, using a Langevin thermostat and Monte Carlo barostat. In each of these simulations, we performed 5 ns of unrestrained equilibration followed by a 1.1-6.7 μs production run.

Simulations used periodic boundary conditions, and a time step of 4.0 fs, with hydrogen mass repartitioning (Hopkins et al., 2015). Bond lengths to hydrogen atoms were constrained using SHAKE. Non-bonded interactions were cut off at 9.0 Å, and long-range electrostatic interactions were computed using the particle mesh Ewald (PME) method with an Ewald coefficient β of approximately 0.31 Å and B-spline interpolation of order 4. The FFT grid size was chosen such that the width of a grid cell was approximately 1 Å.

Analysis protocols for MD simulations

Trajectory snapshots were saved every 200 ps during production simulations. Trajectory analysis was performed using VMD (Humphrey et al., 1996) and CPPTRAJ (Roe and Cheatham, 2013), and visualization was performed using VMD.

Root mean square fluctuation (RMSF) values shown in Figure 4F measure the extent to which an atom fluctuates about its average position in simulation. The first 1 μs of each simulation trajectory was omitted from this analysis to avoid including any initial relaxation or equilibration of the system in the measurement (see Figure S2B). Trajectories were aligned to the initial crystal structure on all transmembrane helix Cα atoms. For each simulation condition, an average structure was generated by considering trajectory snapshots from all simulations under that condition. The RMSF for each Cα atom was then calculated for each trajectory under that condition relative to this average structure using VMD's Python scripting functionality. Each bar in Figure 4F represents a mean of the RMSF values for the simulations under one condition.

Homology modeling of 5-HT$_{2A}$R

Sequence alignment for construction of 5-HT$_{2A}$R homology models was generated with PROMALS3D (Pei and Grishin, 2014), using sequences of human 5-HT$_{2A}$R (Uniprot accession number: P28223), 5-HT$_{2B}$R (P41595), as well as sequences of all available 5-HT$_{2B}$R

X-ray structures [PDB: 4IB4 (chain A) (Wacker et al., 2013), 4NC3 (chain A) (Liu et al., 2013), 5-HT_{2B}R/LSD complex (chain A; current work)]. The alignment was manually edited to remove the amino and carboxy termini that extended past the template structure, and to remove the engineered apocytochrome b562 RIL (BRIL) from the template. A total of 1000 homology models were built using MODELER-9v15 (Webb and Sali, 2014), based on the crystal structure of 5-HT_{2B}R in complex with LSD as the template. LSD was retained in the modeling process to ensure a ligand-competent orthosteric site. Models were then evaluated for their ability to enrich known 5-HT_{2A}R ligands over property-matched decoys through docking to the orthosteric binding site, using DOCK 3.7(Coleman et al., 2013) (see details below). Decoy molecules share the physical properties of known ligands, but are topologically distinct from them and so unlikely to bind, thus controlling for the enrichment of molecules by physical properties alone. For this aim, 34 known ligands with MW < 350 were extracted from the IUPHAR database (Southan et al., 2016), and 1899 property-matched decoys were generated using the DUD-E server (Mysinger et al., 2012). The models were ranked on the basis of their adjusted logAUC and the enrichment factor at 1% of the database. Models also had to reproduce the crystallographic pose of LSD in the template structure and form key interactions with the receptor such as the observed salt bridge with $Asp^{3.32}$. The selected best scoring model in terms of ligand enrichment was further optimized through minimization with the AMBER protein force field and the GAFF ligand force field supplemented with AM1BCC charges (Case et al., 2015).

Molecular docking of LSD and its derivatives

LSD and its derivatives (*S*,*S*)-Azetidide (SSAz), (*R*,*R*)-Azetidide (RRAz) and lysergamide (LSA) were docked to the orthosteric binding pocket of the 5-HT_{2A}R homology model and the 5-HT_{2B}R crystal structure using DOCK3.7 (Coleman et al., 2013). DOCK3.7 places pre-generated flexible ligands into the binding site by superimposing atoms of each molecule on matching spheres, representing favorable positions for individual ligand atoms. Here, 45 matching spheres were used, based on the crystallized LSD pose. The resulting docked ligand poses were scored by summing the receptor-ligand electrostatics and van der Waals interaction energies, and corrected for context-dependent ligand desolvation. Receptor structures were protonated using Reduce (Word et al., 1999). Partial charges from the united-atom AMBER (Case et al., 2015) force field were used for all receptor atoms. Grids which evaluate the different energy terms of the DOCK scoring function were precalculated using AMBER (Case et al., 2015) for the van der Waals term, QNIFFT (Gallagher and Sharp, 1998; Sharp, 1995) (an adaptation of DELPHI) for electrostatics, and ligand desolvation (Mysinger and Shoichet, 2010). Ligands were protonated with Marvin (version 15.11.23.0, ChemAxon, 2015; https://www.chemaxon.com), at pH 7.4. Each protomer was rendered into 3D using Corina (Sadowski et al., 1994) (Molecular Networks GmbH) and conformationally sampled using Omega (Hawkins et al., 2010) (OpenEye Scientific Software). Ligand charges and initial solvation energies were calculated using AMSOL (Chambers et al., 1996; Li et al., 1998).

QUANTIFICATION AND STATISTICAL ANALYSIS

Dose response, log(τ/K_A) calculation and ligand bias quantification

In detail, normalized dose-response data with 5-HT as the reference ligand were fit using the Black and Leff operational model in Graphpad Prism 5.0, where E_{MAX} represents the maximum response of the system and was set to 100, K_A is the functional dissociation constant for the agonist, and τ is the efficacy of the agonist in the given pathway, and *n* is the slope of the response. Data for LSD was fit globally with 5-HT responses such that E_{MAX} and *n* are shared parameters and K_A and τ are then fit individually for LSD. Transduction coefficients (log (τ/K_A)) were calculated using the Black and Leff operational model (Black and Leff, 1983) in Graphpad Prism 5.0. Using 5-HT as the full agonist reference, transduction coefficients for Gq calcium flux and Tango β-Arrestin2 translocation were calculated and averaged across experiments (n = 3). For time-dependent estimates of IP accumulation and β-Arrestin2 BRET translocation, transduction coefficients were calculated for each time point and averaged across experiments (n = 3). Calculation of bias factors utilized the method by Kenakin et al. (Kenakin et al., 2012), where the $\Delta\log(\tau/K_A)$ was calculated relative to the reference 5-HT and the $\Delta\Delta\log(\tau/K_A)$ was calculated by subtracting the Gq transduction coefficient from the β-Arrestin2 transduction coefficient.

DATA AND SOFTWARE AVAILABILITY

Data Resources

HKL2000 was used to process the raw diffraction data and different software found in the phenix and ccp4 software suites were then used to determine, refine, and build the structural model. All software used are reported in Method Details and indicated in the Key Resources Table. The accession number for the coordinates and structures factors of 5-HT_{2B}R/LSD complex reported in this paper is PDB: 5TVN

Cell

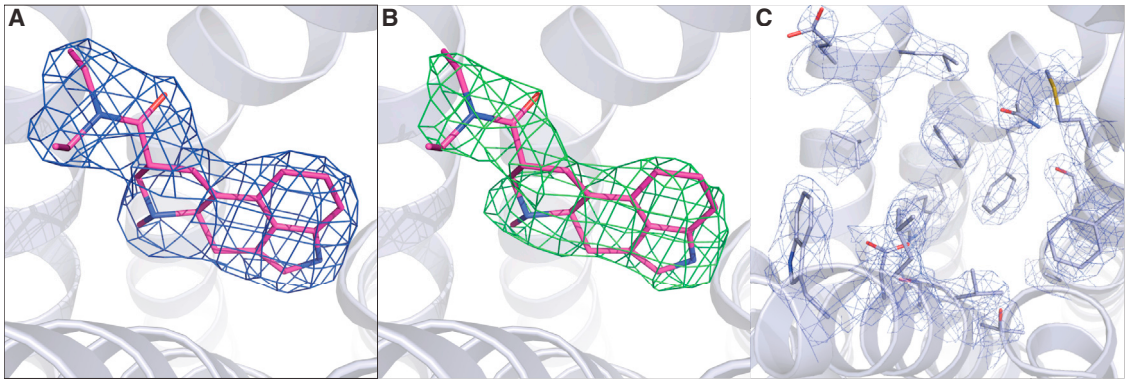

Figure S1. Electron Density of LSD and Ligand Binding Pocket Residues, Related to Figure 1

(A) Structure of LSD (magenta) bound 5-HT_{2B}R (lightblue) with 2Fo-Fc electron density map of LSD (blue mesh) contoured at 1σ. (B) Structure of LSD bound 5-HT_{2B}R with Fo-Fc omit electron density map of LSD (green mesh) contoured at 3σ. (C) 2Fo-Fc electron density map of 5-HT_{2B}R binding pocket residues (blue mesh) contoured at 1σ.

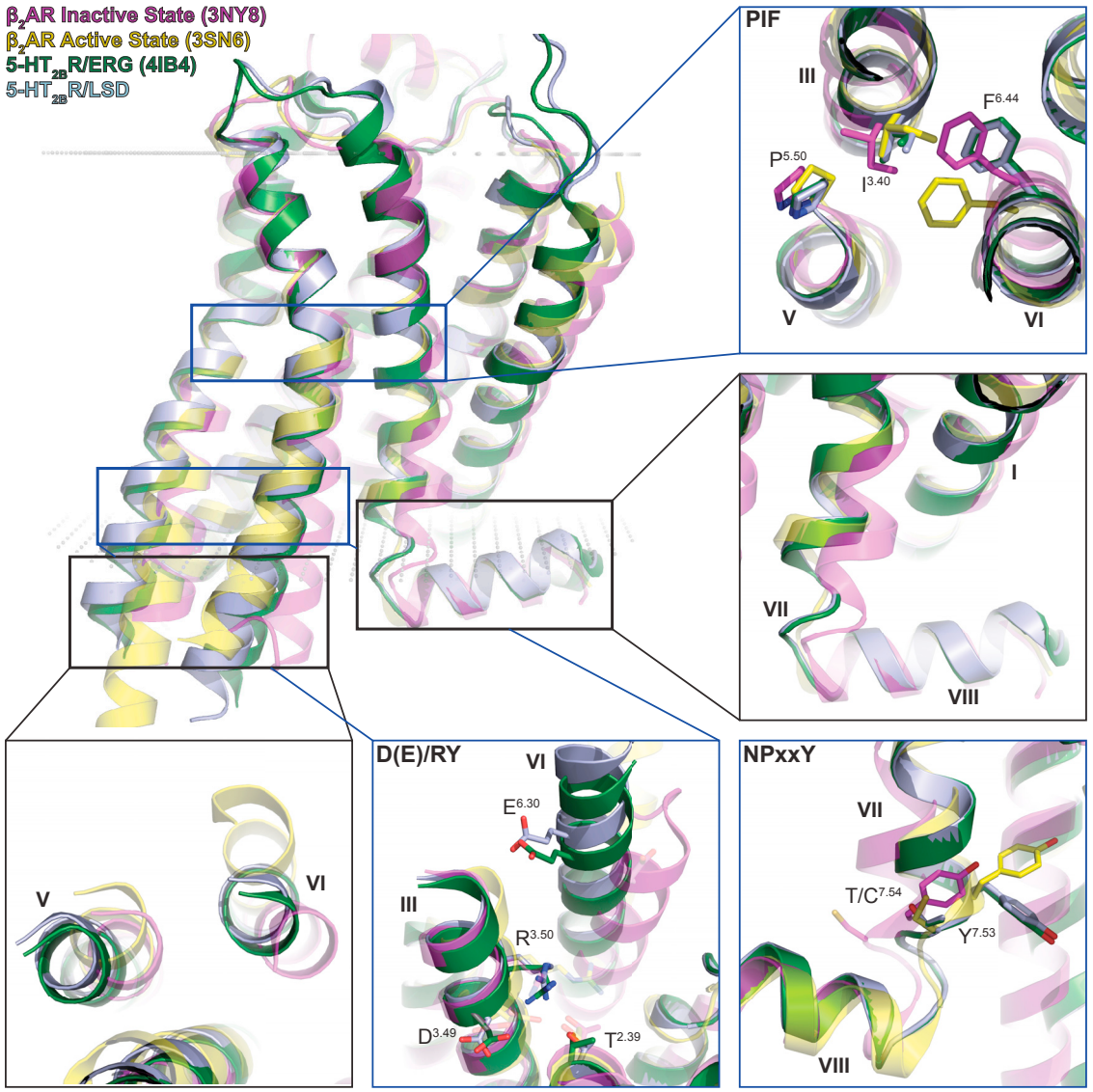

Figure S2. Activation States of 5-HT$_{2B}$R/LSD and 5-HT$_{2B}$R/ERG through Comparison with the β_2 Adrenergic Receptor, Related to Figure 2

Superposition of 5-HT$_{2B}$R/LSD (light blue), 5-HT$_{2B}$R/ERG (dark green) (PDB ID: 4IB4 (Wacker et al., 2013)), β_2AR/ICI 118,551 (transparent magenta) (PDB ID: 3NY8 (Wacker et al., 2010)), and the β_2AR-Gs complex (transparent yellow) (PDB ID: 3SN6 (Rasmussen et al., 2011b)) aligned through helices I-IV. Close ups highlight activation related changes in the PIF, D(E)/RY, and NPxxY motifs, as well as activation related movements in the cytoplasmic portions of helix V, VI, and VII. For better illustration of a cytoplasmic view of helix V, VI, and D(E)/RY, as well as an extracellular view of the PIF motif, parts of the receptors were removed. Membrane boundaries are indicated by gray dots according to the Orientations of Proteins in Membranes database (Lomize et al., 2006).

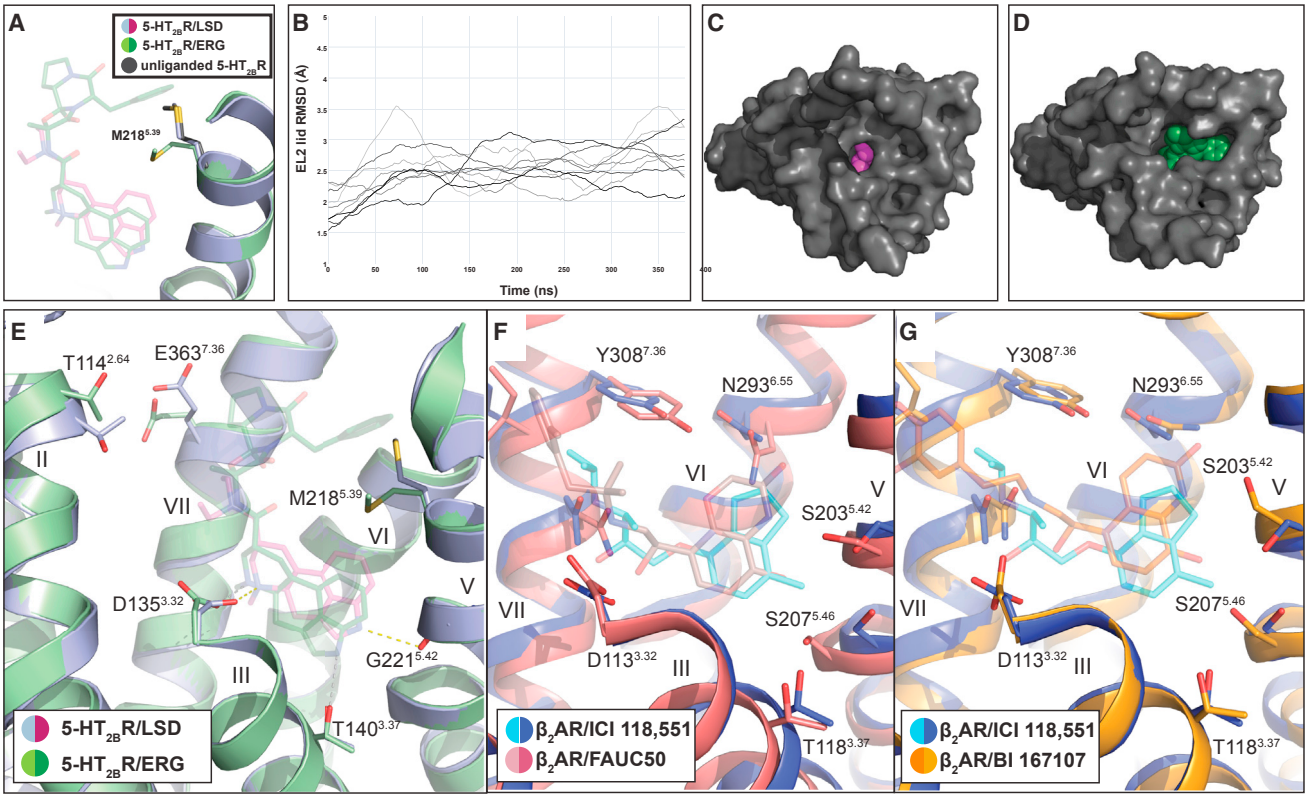

Figure S3. MD Simulations of 5-HT$_{2B}$R Complexes, Differences in LSD versus Ergotamine Surfaces, and Conformational Changes between 5-HT$_{2B}$R/LSD and 5-HT$_{2B}$R/ERG Binding Pockets Compared with Activation-Related Changes Observed in the β_2AR Binding Pocket, Related to Figures 2 and 4

(A) MD simulations suggest that the LSD-bound conformation of M218$^{5.39}$ matches its unliganded conformation, as M218$^{5.39}$ adopts the conformation observed in the LSD-bound crystal structure in simulations initiated from both the ERG-bound and LSD-bound structures but with the ligand removed. The conformations shown for LSD-bound and ERG-bound 5-HT$_{2B}$R are from crystal structures. The conformation shown for unliganded 5-HT$_{2B}$R is from simulations. (B) Convergence analysis for MD simulations of L209A^{EL2} 5-HT$_{2B}$R. Each trace represents the root mean square deviation (RMSD) of the EL2 lid from the LSD-bound crystal structure in a simulation of the LSD-bound L209A^{EL2} mutant. At the beginning of each simulation, the RMSD increases, indicating that the lid is relaxing away from its initial conformation, partly as a result of the mutation. However, this increase levels off within the first 300 ns of simulation. RMSD is computed over all non-hydrogen atoms of residues 207–214. Traces are smoothed by a 60-ns moving average. Note that EL2 continues to fluctuate even when its RMSD from the initial structure is no longer systematically increasing, and that this analysis does not demonstrate convergence in the strict sense that each simulation fully samples the Boltzmann distribution. We performed multiple simulations under each condition, and Figure 4F shows aggregate statistics across these simulations. (C) Shows surface representation of 5-HT$_{2B}$R/LSD complex with LSD in magenta while (D) shows surface representation of 5-HT$_{2B}$R/ERG complex with ERG in green. (E) Superposition of ligand binding sites of 5-HT$_{2B}$R (light blue) bound to LSD (transparent magenta), and 5-HT$_{2B}$R (light green) bound to ERG (transparent dark green)(PDB ID: 4IB4 (Wacker et al., 2013)). (F) Superposition of ligand binding sites of the inactive state β_2AR (purple) bound to the inverse agonist ICI 118,551 (transparent cyan) (PDB ID: 3NY8 (Wacker et al., 2010), and inactive state β_2AR (salmon) bound to the covalent agonist FAUC50 (transparent light pink)(PDB ID: 3PDS (Rosenbaum et al., 2011)). (G) Superposition of ligand binding sites of the inactive state β_2AR (purple) bound to the inverse agonist ICI 118,551 (transparent cyan) (PDB ID: 3NY8 (Wacker et al., 2010), and the active state β_2AR (dark yellow) bound to the agonist BI 167107 (transparent orange pink)(PDB ID: 3P0G (Rasmussen et al., 2011a)). For the 5-HT$_{2B}$/ERG versus 5-HT$_{2B}$/LSD the ligand-binding pocket RMSD is 0.99 Å while for the active versus inactive β_2AR structures the RMSD is 0.85 Å. The RMSD values were computed over all non-hydrogen backbone and side-chain atoms in transmembrane helix residues that are in the union of (i) the LSD-binding pocket and the ERG-binding pocket for 5-HT$_{2B}$R and (ii) the ICI 118,551-binding pocket and the BI-binding pocket for β_2AR (binding pocket residues are defined as those within 4.5 Å of the ligand in the crystal structure).

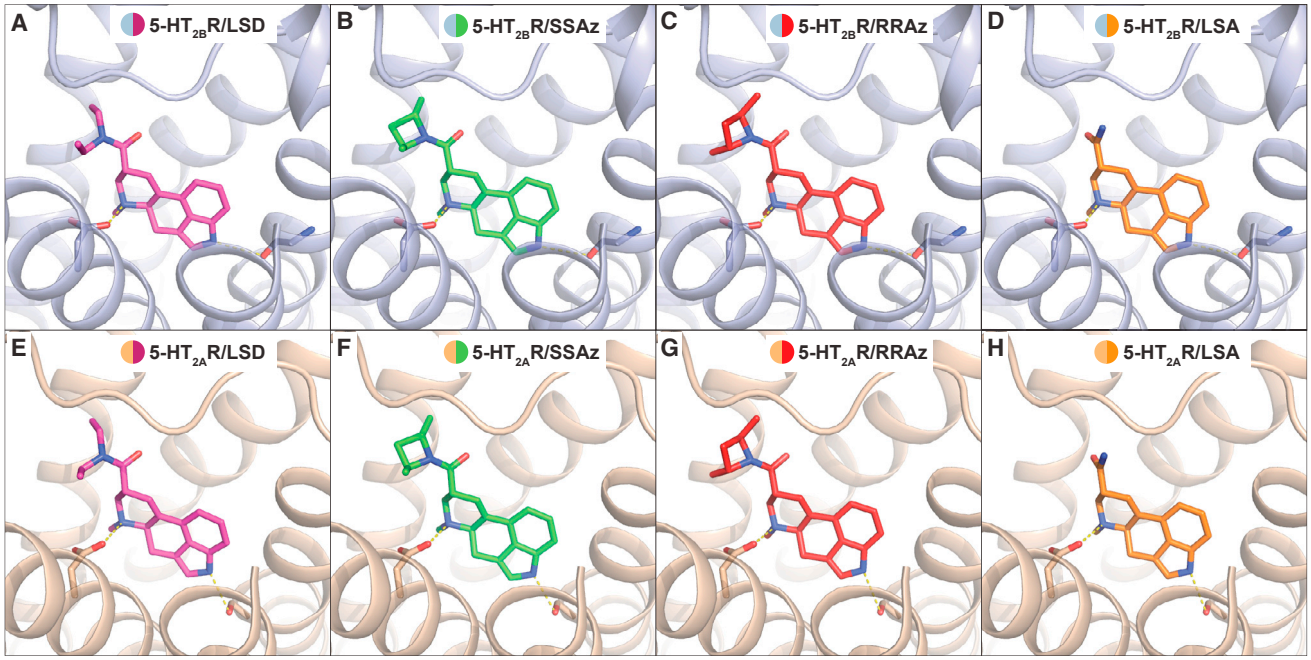

Figure S4. Docking of LSD Derivatives into 5-HT$_{2B}$R Structure and 5-HT$_{2A}$R Homology Model, Related to Figure 3

(A) Close up view of the orthosteric binding site of 5-HT$_{2B}$R/LSD complex structure with LSD in magenta and receptor in light blue. (B) SSAz (green) docked into orthosteric site of 5-HT$_{2B}$R (light blue). (C) RRAz (red) docked into orthosteric site of 5-HT$_{2B}$R (light blue). (D) Lysergamide (orange) docked into orthosteric site of 5-HT$_{2B}$R (light blue). (E) LSD (magenta) docked into orthosteric site of 5-HT$_{2A}$R homology model (wheat). (F) SSAz (green) docked into orthosteric site of 5-HT$_{2A}$R homology model (wheat). (G) RRAz (red) docked into orthosteric site of 5-HT$_{2A}$R homology model (wheat). (H) Lysergamide (orange) docked into orthosteric site of 5-HT$_{2A}$R homology model (wheat). Hydrogen bonds between basic amines of the ergolines and the conserved aspartate of 5-HT$_{2A}$R and 5-HT$_{2B}$R are shown as yellow dashes. In 5-HT$_{2B}$R, compounds form an additional hydrogen bond between the indole nitrogen and the backbone keto group of G221$^{5.42}$, whereas in 5-HT$_{2A}$R compounds form a hydrogen bond between the indole nitrogen and the sidechain of S242$^{5.42}$.

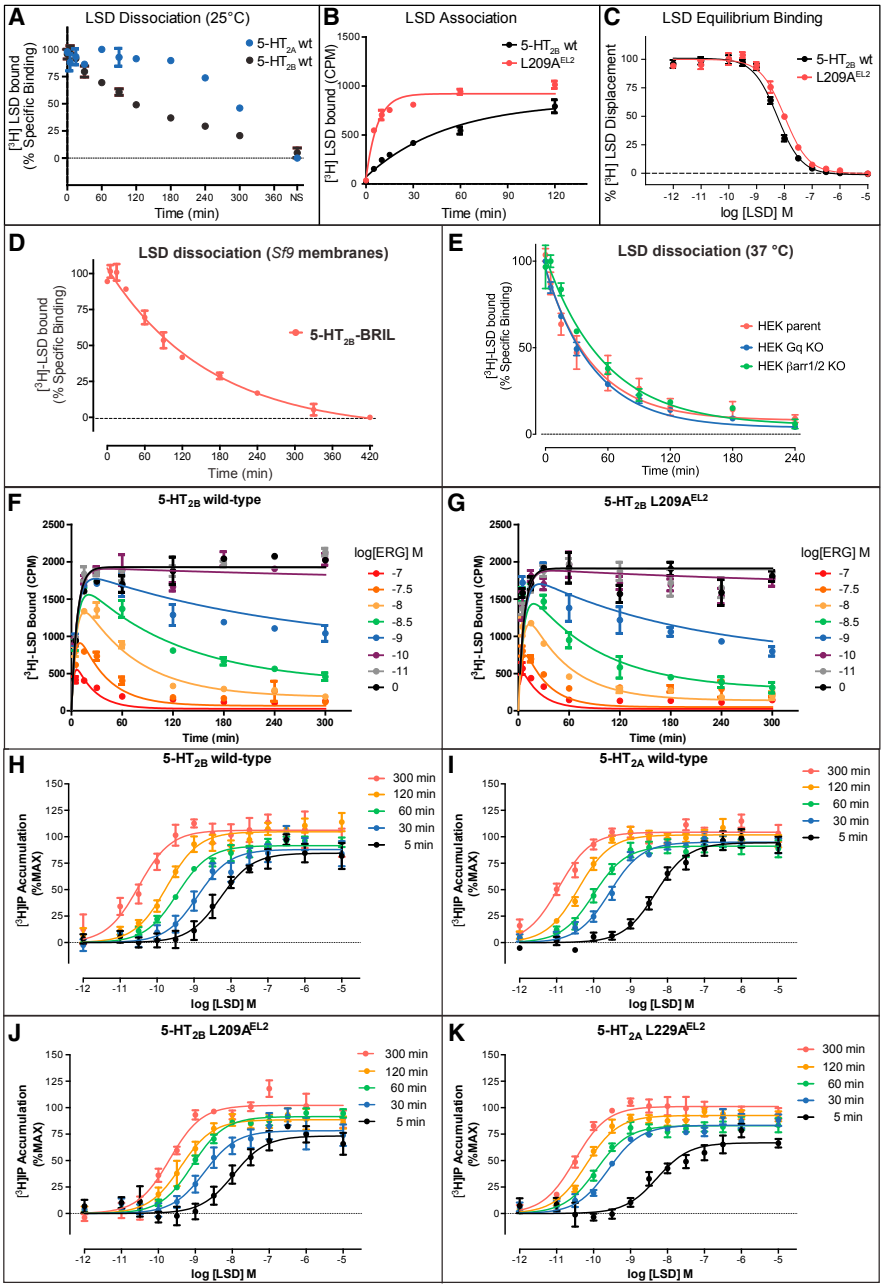

Figure S5. LSD Binding and Signaling Kinetics, Related to Figures 4 and 5

(A) [^{3}H]-LSD dissociation at 5-HT$_{2B}$R (black circles) and 5-HT$_{2A}$R (blue circles) performed at 25°C shows that LSD does not fully dissociate from the receptors at 5 hr/300 min; NS is non-specific binding defined as [^{3}H]-LSD binding in the presence of 10 μM SB206553 (5-HT$_{2B}$R) or 10 μM spiperone (5-HT$_{2A}$R). Data represent n = 3 performed in duplicate. (B) [^{3}H]-LSD association to 5-HT$_{2B}$R wt (black circles) and 5-HT$_{2B}$R L209A^{EL2} mutant (red circles) performed at 37°C, show accelerated on-rate of [^{3}H]-LSD at mutant receptor. Data represent n = 2 performed in duplicate. (C) LSD equilibrium binding shows that the affinity of LSD at L209A^{EL2} compared to wild-type 5-HT$_{2B}$R is not substantially affected. Data represent n = 2 performed in duplicate. (D) [^{3}H]-LSD dissociation from crystallized 5-HT$_{2B}$R construct expressed in Sf9 insect cell membranes. (E) [^{3}H]-LSD dissociation from 5-HT$_{2B}$R expressed in Gq-knock out, arrestin-knock out, or parental HEK cell line. Ergotamine (ERG) binding kinetics at 5-HT$_{2B}$R (F) and L209A^{EL2} (E) in the presence [^{3}H]-LSD indicating that the slow off-rate of ERG does not change significantly comparing wild-type to mutant (n = 2). (H) Time-dependent change in Gq-mediated IP accumulation for 5-HT$_{2B}$R (n = 3). (I) Time-dependent change in Gq-mediated IP accumulation for 5-HT$_{2B}$R L209A^{EL2} (n = 3). (J) Time-dependent change in Gq-mediated IP accumulation for 5-HT$_{2A}$R (n = 3). (K) Time-dependent change in Gq-mediated IP accumulation for 5-HT$_{2A}$R L229A^{EL2} (n = 3).